

## Article

# Electrochemical Performances of Li-Ion Batteries Based on LiFePO<sub>4</sub> Cathodes Supported by Bio-Sourced Activated Carbon from Millet Cob (MC) and Water Hyacinth (WH)

Wend-Waoga Anthelme Zemane and Oumarou Savadogo \*

Laboratory of New Materials for Energy and Electrochemistry, Polytechnique Montreal, Montreal, QC H3T 1J4, Canada; wend-waoga-anthelme.zemane@polymtl.ca

\* Correspondence: osavadogo@polymtl.ca; Tel.: +1-514-340-4725

## Abstract

The electrochemical performance of Li-ion batteries employing LiFePO<sub>4</sub> (LFP) cathodes supported by bio-sourced activated carbon derived from millet cob (MC) and water hyacinth (WH) were systematically investigated. Carbon activation was carried out using potassium hydroxide (KOH) at varying mass ratios of KOH to precursor material: 1:1, 2:1, and 5:1 for both WH and MC-derived carbon. The physical properties (X-ray diffraction patterns, BET surface area, micropore and mesopore volume, conductivity, etc.) and electrochemical performance (specific capacity, discharge at various current rates, electrochemical impedance measurement, etc.) were determined. Material characterization revealed that the activated carbon derived from MC exhibits an amorphous structure, whereas that obtained from WH is predominantly crystalline. High specific surface areas were achieved with activated carbons synthesized using a low KOH-to-carbon mass ratio (1:1), reaching  $413.03\text{ m}^2\cdot\text{g}^{-1}$  for WH and  $216.34\text{ m}^2\cdot\text{g}^{-1}$  for MC. However, larger average pore diameters were observed at higher activation ratios (5:1), measuring 8.38 nm for KOH/WH and 5.28 nm for KOH/MC. For both biomass-derived carbons, optimal electrical conductivity was obtained at a 2:1 activation ratio, with values of  $14.7 \times 10^{-3}\text{ S}\cdot\text{cm}^{-1}$  for KOH/WH and  $8.42 \times 10^{-3}\text{ S}\cdot\text{cm}^{-1}$  for KOH/MC. The electrochemical performance of coin cells based on cathodes composed of 85% LiFePO<sub>4</sub>, 8% of these activated carbons, and 7% polyvinylidene fluoride (PVDF) as a binder, with lithium metal as the anode were studied. The LiFePO<sub>4</sub>/C (LFP/C) cathodes exhibited specific capacities of up to  $160\text{ mAh}\cdot\text{g}^{-1}$  at a current rate of C/12 and  $110\text{ mAh}\cdot\text{g}^{-1}$  at 5C. Both LFP/MC and LFP/WH cathodes exhibit optimal energy density at specific values of pore size, pore volume, charge transfer resistance ( $R_{ct}$ ), and diffusion coefficient ( $D_{Li}$ ), reflecting a favorable balance between ionic transport, accessible surface area, and charge conduction. Maximum energy densities relative to active mass were recorded at  $544\text{ mWh}\cdot\text{g}^{-1}$  for LFP/MC 2:1,  $554\text{ mWh}\cdot\text{g}^{-1}$  for LFP/WH 2:1, and  $568\text{ mWh}\cdot\text{g}^{-1}$  for the reference LFP/graphite system. These performance results demonstrate that the development of high-performing bio-sourced activated carbon depends on the optimization of various parameters, including chemical composition, specific surface area, pore volume and size distribution, as well as electrical conductivity.



Academic Editors: Binghui Xu and Haichao Chen

Received: 15 May 2025

Revised: 1 September 2025

Accepted: 7 September 2025

Published: 30 September 2025

**Citation:** Zemane, W.-W.A.; Savadogo, O. Electrochemical Performances of Li-Ion Batteries Based on LiFePO<sub>4</sub> Cathodes Supported by Bio-Sourced Activated Carbon from Millet Cob (MC) and Water Hyacinth (WH). *Batteries* **2025**, *11*, 361. <https://doi.org/10.3390/batteries11100361>

**Copyright:** © 2025 by the authors. Licensee MDPI, Basel, Switzerland. This article is an open access article distributed under the terms and conditions of the Creative Commons Attribution (CC BY) license (<https://creativecommons.org/licenses/by/4.0/>).

**Keywords:** LiFePO<sub>4</sub>; lithium; activated carbon; water hyacinth; millet cob; porosity; coin cells; cycling performance; specific capacity; electrochemical impedance spectroscopy

## 1. Introduction

The Lithium iron phosphate has emerged as a cost-effective and promising positive electrode for lithium-ion batteries, particularly suited for applications in electronics, telecommunications, transportation, and beyond. Since its introduction as a cathode [1], LiFePO<sub>4</sub> has demonstrated numerous advantages, including a highly theoretical capacity (170 mAh/g), exceptional longevity, an excellent stable discharge profile, the ability to handle high current rates, moderate or low cost, natural presence of its constituent elements on earth, excellent thermal and chemical stability and more environmentally friendly utilization than the other cathode-based materials [2–4]. Its thermal stability, attributed to its phospho-olivine structure, is rooted in a unique crystalline configuration: oxygen atoms form a hexagonal close-packed lattice, iron ions create zigzag chains of octahedra connected by phosphate (PO<sub>4</sub>) groups, and Li<sup>+</sup> ions occupy octahedral sites arranged in one-dimensional tunnels along the [010] axis [1–3,5]. The P<sup>5+</sup> ions create strong covalent bonds with oxygen and confer high structural stability, enhancing thermal resistance and ensuring reliable performance at elevated temperatures, a critical advantage for demanding applications. Additionally, it has been shown that [6] the combination of phosphorus and iron optimizes redox energy, generating a voltage of 3.4 V relative to Li/Li<sup>+</sup>, a key factor for stable electrochemical performance. The excellent reversibility of LiFePO<sub>4</sub> is linked to the structural similarity between LiFePO<sub>4</sub> and FePO<sub>4</sub> [6]. During the phase transition between these two states during de-lithiation, changes in crystal parameters remain minimal, with a volume reduction of only 6.8% and a density increase of 2.6%, reducing structural stress during charge-discharge cycles [3]. Composed of naturally abundant elements such as iron, lithium, and phosphorus, LiFePO<sub>4</sub> could reduce cathode costs by 10–50% of the total lithium-ion battery cost, enhancing its competitiveness for large-scale commercial applications [3,7].

Despite its many advantages, certain limitations hinder the widespread adoption of LiFePO<sub>4</sub>. Its low ionic diffusivity ( $\sim 10^{-14}$  cm<sup>2</sup>/s) and poor electronic conductivity ( $\sim 10^{-9}$  S/cm) limit its performance during rapid charge and discharge cycles. This low electronic conductivity was attributed to the bonding structure of iron atoms: FeO<sub>6</sub> octahedra share vertices rather than edges or faces, increasing the distance between iron atoms and complicating electron transport [2,8]. Another limitation of this cathode material is its low operating voltage which is not higher than 3.4 V vs. Li/Li<sup>+</sup> whereas the other commercial cathodes exhibit potentials closer to 4 V vs. Li/Li<sup>+</sup>. To address these drawbacks, various approaches have been developed, including particle size reduction [9–11], doping with metals [9,12,13], and coating LiFePO<sub>4</sub> particles with carbon [9,14–17]. These methods improve electronic conductivity and overall performance, though they may incur additional costs. Issues are also related to the long-term stability of the dopant. Ongoing research aims to identify innovative and cost-effective solutions to optimize LiFePO<sub>4</sub> performance and stability while controlling expenses [18].

On the particle size reduction, it has been noted [19] that nanomaterials exhibit excellent mechanical stress resistance, facilitating adaptation to volume changes during charge-discharge cycles while improving lithium-ion diffusion and electron transfer due to reduced diffusion distances. However, their highly specific surface area makes them susceptible to undesirable side reactions, such as electrolyte degradation, which can affect chemical stability. Moreover, excessively small particle sizes may reduce electronic conductivity and lead to agglomeration, complicating processing and incorporation into composite materials [20–22]. Metal doping has proven effective in enhancing Li<sup>+</sup> ion diffusion and cathode conductivity [22–25]. It has been shown that integrating super-valent ions [22], such as Mg<sup>2+</sup>, Al<sup>3+</sup>, or Ti<sup>4+</sup>, can increase electronic conductivity by orders of magnitude by creating p- and n-type semiconducting regions. It has been shown that

partial replacement of  $\text{Fe}^{2+}$  with  $\text{Mn}^{2+}$  improves conductivity, achieving a specific capacity exceeding 140 mAh/g with minimal performance loss over cycles [3,8]. Additionally, it has been confirmed that doping with precious metals like platinum and palladium significantly enhances electrochemical properties [13,23–25]. On the contrary, it has been noted that aliovalent doping is poorly tolerated by the olivine structure of  $\text{LiFePO}_4$ , as dopant ions are not always well integrated into the crystal lattice, limiting their effectiveness in improving electronic conductivity [26,27]. To overcome the conductivity limitations of  $\text{LiFePO}_4$  cathodes, it has been suggested [28] to use conductive carbon-based materials as supports, promoting optimal lithium-ion flow and enhancing electrochemical performance. Several studies [19,29–34] have explored the application of carbon coatings at varying percentages to strengthen conductivity and optimize overall cathode performance.

More recently, several studies have focused on the improvement of the performances of  $\text{LiFePO}_4$  cathodes. A study explored the effect of holes created by a picosecond pulsed laser on the high-rate performance of a hybrid  $\text{LiFePO}_4$ /activated carbon electrode [35]. Another research effort involved wrapping  $\text{LiFePO}_4$  particles with a combination of activated carbon and reduced graphene oxide, yielding cathodes with remarkably high capacities and specific energy densities [36]. A separate investigation prepared LFP/C composites with varying carbon contents via the carbothermal reduction method. Accordingly, it was found that the amount of carbon significantly influences the material properties: increasing the carbon content led to smaller and more uniformly distributed particles. Among the tested samples, the LFP/C-15 composite exhibited the best electrochemical performance, achieving a discharge capacity of  $160.7 \text{ mAh g}^{-1}$  after 100 cycles at 0.1 C, and maintaining a capacity retention of 82.1% [37].

This innovative study explores the use of additives bio-sourced carbon derived from agricultural waste, such as millet cob (MC) and water hyacinth (WH), to develop  $\text{LiFePO}_4$  (LFP) cathodes for lithium batteries. These novel materials, applied in this context for the first time, are expected to provide new scientific insights on the correlation which might exist between the physicochemical properties and the improvements in the electrochemical parameters of LFP cathodes enhanced with additives bio-derived carbon from MC and WH. This research will help to advance in the understanding of bio-sourced carbon additives influence the performance of LFP-based cathodes in lithium-ion batteries.

## 2. Materials and Methods

### 2.1. Materials, Electrodes, Li-Ion Battery Cell Elaboration and Fabrications

The millet cob and water hyacinth samples were weighed using an analytical balance and placed in refractory crucibles. A furnace operating under an argon atmosphere was used both for drying and for determining the volatile matter and ash content. The obtained ash of millet cob and water hyacinth samples were chemically activated using potassium hydroxide (KOH) as the activating agent. Three different concentrations were investigated: 10% KOH (KOH/CM 1:1), 20% KOH (KOH/CM 2:1), and 50% KOH (KOH/CM 5:1). Accordingly, the activated carbon samples derived from millet cob were labeled KOH/MC 1:1, KOH/MC 2:1, and KOH/MC 5:1, while those from water hyacinth were referred to as KOH/WH 1:1, KOH/WH 2:1, and KOH/WH 5:1. The synthetic graphite powder (99.99% purity), used as a reference material, was supplied by Sigma Aldrich, Oakville, ON, Canada.

The working anode electrodes were prepared by mixing 85 wt% synthesized activated carbon, 8 wt% carbon black, and 7 wt% polyvinylidene fluoride (PVDF) binder dissolved in N-methyl-2-pyrrolidone (NMP) to form a homogeneous slurry. The slurry was uniformly coated onto copper foil current collectors and dried under vacuum at 120 °C for 12 h to remove residual solvent. Circular electrodes (12 mm diameter) were punched from the

coated foil prior to assembly. CR2032-type coin half-cells were assembled in an argon-filled glovebox using lithium metal foil as the counter/reference electrode.

Galvanostatic charge–discharge tests of the anodes were conducted at a current rate of C/24 (based on theoretical graphite capacity) within a potential window of 0.01–3.0 V vs. Li<sup>+</sup>/Li, using a potentiostat/galvanostat. This low rate minimizes parasitic side reactions and enables accurate probing of the intrinsic Li-storage behavior of the carbons.

Cathode Electrodes were fabricated using LFP powder, with a purity of more than 99% and particle size less than 5 microns (Sigma Aldrich) and lithium metal discs (MSE Supplies). A polymeric binder, polyvinylidene fluoride (PVDF), dissolved in dimethylacetamide (DMAC), was used to homogenize and coat the active LiFePO<sub>4</sub>/carbon (LFP/C) mixture onto an aluminum current collector. The electrode composition consisted of 85% LFP, 8% activated carbon or graphite, and 7% PVDF dissolved in DMAC at 60 °C. The cathode electrode assembly was also carried out in CR2032 coin cell using standard components, including casings, springs, spacers, and gaskets.

All assembly steps were performed in an argon-filled glove box to prevent exposure to moisture and oxygen.

For the separate characterization of both anode or cathode electrodes, the electrolyte, supplied by Sigma Aldrich, consisted of a 1 M solution of LiPF<sub>6</sub> dissolved in an equimolar mixture of ethylene carbonate (EC), dimethyl carbonate (DMC), and ethyl methyl carbonate (EMC), ensuring high ionic conductivity and thermal stability for lithium-ion battery operation. A 25 μm-thick microporous polypropylene membrane (Celgard® 2400) was used as the separator, cut into 1.90 cm discs to fit the dimensions of the coin cells.

## 2.2. Methods

### 2.2.1. X-Ray Diffraction (XRD)

The crystalline phase, structural characteristics, and purity of the synthesized powder were analyzed using a Bruker D8 X-ray diffractometer equipped with a CuK $\alpha$  radiation source ( $\lambda = 0.15406$  nm,  $E = 8.04867$  keV). The measurements were conducted in  $\theta$ –2  $\theta$  geometry, with a scanning range from 5° to 80° (2  $\theta$ ), a step size of 0.02°, and an angular sweep rate of 0.02°/s.

### 2.2.2. Specific Surface Area Determination Using BET Technic

The specific surface area ( $S_{\text{BET}}$ ), pore volume, and pore size distribution (PSD) of the various samples were characterized using the Brunauer–Emmett–Teller (BET) method. These measurements were conducted with a Quantachrome AS1Win™ automated gas sorption analyzer, which utilizes acquisition and reduction software for data collection and analysis.

Prior to analysis, the LFP powder was degassed under dynamic vacuum ( $\leq 10^{-3}$  mbar) at 300 °C for 3 H to eliminate adsorbed impurities. A mass of 791.50 mg was then loaded into the BSD-PM sample tube. The sample was cooled to 77.3 K (liquid nitrogen temperature), and nitrogen adsorption isotherms were measured as a function of relative pressure ( $P/P_0$ ), with  $P_0$  representing the initial pressure (1.0258 bars). BET surface area analysis was performed in the range of  $P/P_0 = 0.05$ –0.30. Subsequently, the pressure was increased to near saturation ( $P/P_0 \approx 0.99$ ) and then gradually decreased to obtain the desorption branch for Barrett–Joyner–Halenda (BJH) mesopore analysis (pore sizes 2–50 nm). Finally, low-pressure adsorption data ( $P/P_0 < 0.01$ ) were collected for Horváth–Kawazoe (HK) micropore characterization (<2 nm).

### 2.2.3. Pore Size Distribution Techniques

Several techniques are available in the literature for characterizing carbonaceous pore systems from BET measurement, including the BJH method [38], HK method [38], SF

(Saito-Foley) method [39], NLDFT (non-local density functional theory) method [40] and MP (Micropore) method [41]. These analytical models provide meaningful insights into the pore architecture of synthesized activated carbons [42]. The HK and SF methods are widely employed for quantifying micropore size distributions, whereas the BJH method is commonly used to assess meso-porosity. NLDFT offers a more comprehensive analysis, capable of simultaneously resolving micropores, mesopores, and macropores [40]. In the present study, micropores were characterized using the HK method, while mesopores and macropores were analyzed via NLDFT, a robust, multi-parametric technique for detailed pore size and pore distribution evaluation.

#### 2.2.4. Surface Morphology Characterisation and Qualitative Chemical Composition Analysis

Scanning electron microscopy (SEM) was used to investigate the surface morphology and microstructure of activated carbon (WH and MC), including particle size and surface characteristics. Imaging was performed using a JEOL JSM-7600F thermal field-emission scanning electron microscope (FE-SEM) from JEOL North America, Peabody, MA, USA, operated at an acceleration voltage of 15–30 kV and a probe current ranging from 0.1 pA to 200 nA. The equipment includes an energy-dispersive X-ray spectroscopy (EDS) detector for elemental mapping and analyzing each component. EDS, a qualitative technique, was employed to identify and characterize the elementary constituents of the synthesized carbon samples [43–45].

#### 2.2.5. Conductivity Measurement of the Activated Carbons

Electrical conductivity was measured using the four-point probe method using a S-302 Four Point Resistivity Probing Equipment from Lucas Labs, Gilroy, CA, USA. This test assesses the conductivity of the activated carbon, a critical property of this electrode material for battery applications.

#### 2.2.6. Electrochemical Studies

The electrochemical performance evaluation was based on the utilization of the following various technics: galvanostatic charge–discharge tests, cycling stability measurements, and electrochemical impedance spectroscopy (EIS). These techniques were used to determine key performance metrics, including specific capacity, Coulombic efficiency, Peukert coefficient, cycling durability of the cathodes, and lithium-ion diffusion coefficients. The results were analyzed to assess the influence of activated carbon properties on cathode behavior and compared to those obtained using graphite, to evaluate the advantages of bio-based carbon materials.

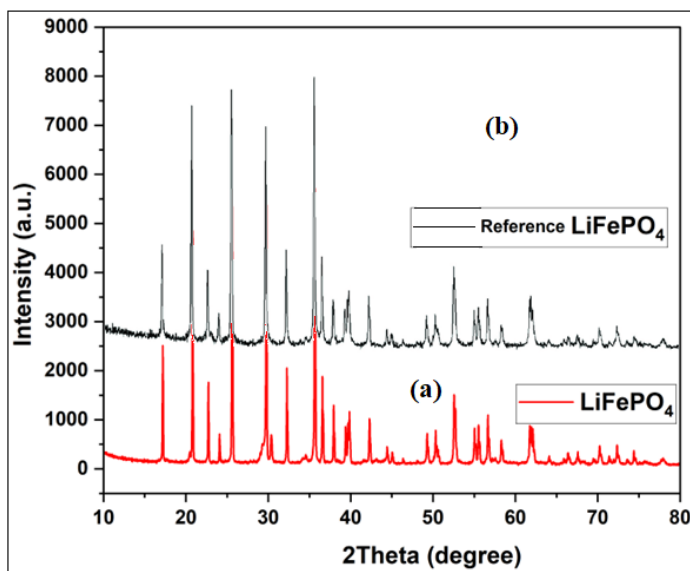
Electrochemical testing of Li-ion coin cell with LFP/C was performed using a Princeton Applied Research 273A potentiostat, a Solartron CellTest 1470 multichannel potentiostat (Scribner, Southern Pines, NC, USA), and a Solartron 1255B frequency response analyzer (Scribner). The 273A potentiostat was employed for cyclic voltammetry analysis, while the Solartron 1470 multichannel potentiostat was used for galvanostatic charge–discharge cycling. The Solartron 1255B analyzer, interfaced with the 273A system, enabled the acquisition of EIS data.

### 3. Results and Discussion

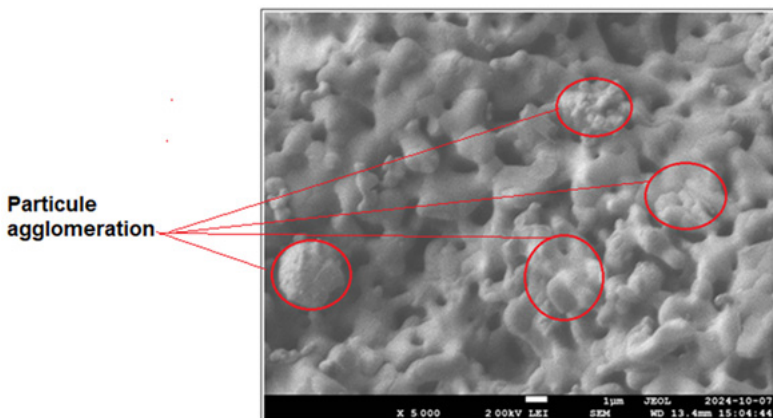
#### 3.1. Morphological and Structural Characterization of Pure LiFePO<sub>4</sub>

Figure 1a displays the XRD pattern of the synthesized LiFePO<sub>4</sub> powder. For comparison, the reference diffraction pattern of pure LiFePO<sub>4</sub>, based on standard card 01-090-1862, is shown in Figure 1b [46]. All diffraction peak positions in Figure 2 closely match those of the LiFePO<sub>4</sub> reference) [46], confirming the successful formation of the LiFePO<sub>4</sub> phase.

Moreover, the sharp and well-defined peaks indicate a high degree of crystallinity and support the presence of the stable triphylite phase. Well-ordered crystalline structures help for optimizing ionic conductivity and facilitate lithium-ion transport by providing well-defined diffusion pathways, which is indispensable for efficient charge/discharge cycling.



**Figure 1.** X-ray Diffractogram of synthesized LiFePO<sub>4</sub> (a) and the standard LFPO<sub>4</sub> (b) [46].



**Figure 2.** SEM Image of the synthesized LiFePO<sub>4</sub> Powder:  $\times 5000$ .

SEM analysis (Figure 2) reveals that the LiFePO<sub>4</sub> particles exhibit relatively uniform morphology, ranging from spherical to ellipsoidal shapes, with particle sizes between 100 nm and 500 nm. However, SEM micrographs also show evidence of particle agglomeration (highlighted by red circles), which could negatively impact cathode performance by limiting electrical conductivity, increasing ion diffusion path lengths, and ultimately reducing overall electrochemical efficiency.

Figure 3 illustrates the nitrogen adsorption–desorption isotherms of LiFePO<sub>4</sub>, showing the variation of the adsorbed volume ( $\text{cm}^3/\text{g}$ ) as a function of relative pressure ( $P/P_0$ ). The hysteresis loop corresponds to type H4 according to IUPAC classification, indicating the coexistence of micropores and mesopores in the material. The initial rise in nitrogen adsorption at low relative pressures suggests the presence of micropores (<2 nm), as these are typically filled first. This is followed by a more pronounced increase in adsorption at higher relative pressures, characteristic of mesoporous structures (2–50 nm). Thus, the isotherm supports the presence of both pore types, with mesopores likely predominating, as inferred from the overall shape of the curve. This porosity suggests a hierarchical pore

structure that may enhance electrolyte accessibility and facilitate ion transport within the electrode material [47].

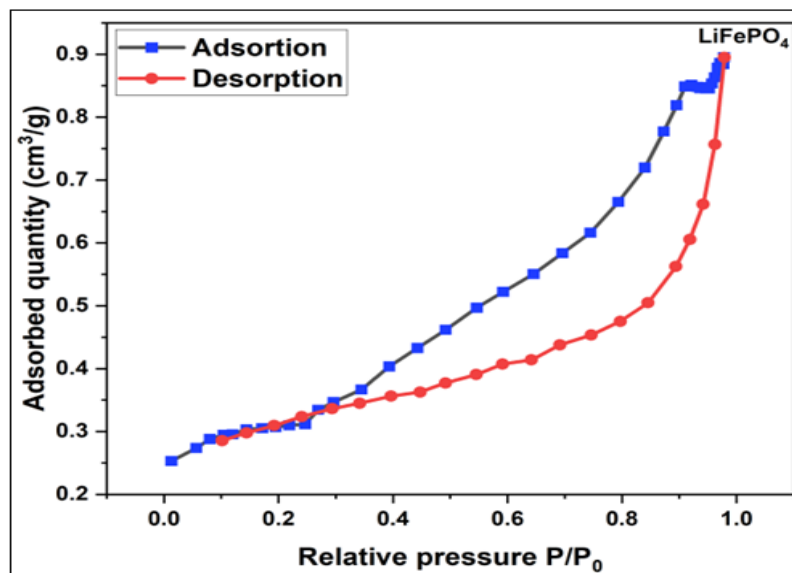


**Figure 3.** Variation of the nitrogen adsorption–desorption volume of  $\text{LiFePO}_4$  ( $\text{cm}^3/\text{g}$ ) as a function of the relative pressure  $P/P_0$ .

The PSD, specifically for mesoporous structures, was evaluated using the Barrett–Joyner–Halenda (BJH) method, which is based on the Kelvin equation (Equation (1)) [48]. This model provides a quantitative framework for converting nitrogen adsorption data into PSD profiles. According to the BJH approach, the radius of the condensate with a hemispherical meniscus ( $r_i$ ), or the curvature radius of the adsorbent surface ( $r_i$ ), is expressed in nanometers and defined as follows:

$$r_i = -\frac{2\sigma V \cos\theta}{RT \ln\left(\frac{P_i}{P_0}\right)} \quad (1)$$

where  $\sigma$  is the liquid surface tension of the adsorbate in  $\text{N}/\text{cm}$ ,  $V$  is the molar volume of the liquid phase in  $\text{ml}/\text{mol}$ ;  $\theta$  is the contact angle between the meniscus and the solid wall in radians;  $R$  is the ideal gas constant ( $8.31 \text{ J}/(\text{mol}\cdot\text{K})$ );  $T$  is the temperature in Kelvin (K);  $P_i$  is the applied pressure in atm;  $P_0$  is the reference pressure in atm;  $P_i/P_0$  is the partial pressure when pressure  $P_i$  is applied to the sample.

From this relation, a set of algorithms is employed to estimate pore structure characteristics at each relative pressure  $P_i/P_0$ , based on nitrogen adsorption–desorption isotherms. These include the pore anisotropy factor  $b_i$ , defined as the ratio of pore length ( $L_i$ ) to pore diameter ( $D_i$ ), that is,  $b_i = L_i/D_i$ . The method also enables the determination of pore surface area ( $S_{p_i}$ ), pore volume ( $V_{p_i}$ ), and pore radius ( $r_i$ ) =  $D_i/2$  at each relative pressure. By plotting  $\log(S_{p_i}^3/V_{p_i})$  vs.  $\log r_i$ , a linear relationship is obtained with slope  $s_i = \alpha_i - 1$  where  $\alpha_i$  is defined as the pore length parameter. This slope is further related to the pore length ( $L_i$ ) via the power law relation:  $L_i = k r_i \alpha_i - 1$ , where  $k$  is a proportionality constant (in grams). Thus,  $\alpha$  serves as a parameter for assessing pore elongation.

For pores narrower than 2 nm, the fluid–solid interaction becomes dominant, necessitating alternative models. In such cases, the pores are classified as micropores, and their filling occurs in the pre-capillary condensation region of the physisorption isotherm. The Horváth–Kawazoe (HK) method offers a specialized approach to determining micropore size distributions. Initially developed for slit-shaped carbonaceous pores, it has since been adapted to account for cylindrical geometries such as those found in silica-based materi-

als. The HK model is founded on the principle that the relative pressure required to fill micropores of a specific shape and size is directly correlated with the adsorbate–adsorbent interaction energy [49].

Based on these energies of interaction, the following equation (Equation (2)) was developed to relate variations in partial pressure to pore dimensions and relevant physical parameters [49].

$$RT\ln\left(\frac{P}{P_0}\right) = K \frac{N_a A_a + N_A + A_A}{\sigma^4(1-d)} \times \left[ \frac{\sigma^4}{3(1-d/2)^3} - \frac{\sigma^{10}}{9(1-d/2)^9} - \frac{\sigma^4}{3(d/2)^3} + \frac{\sigma^{10}}{9(d/2)^9} \right] \quad (2)$$

where: K is Avogadro's constant ( $K = 6.02 \times 10^{23}$  atoms);  $\sigma$  is the distance between a gas atom and the surface at zero energy of interaction, l is the distance from the surface;  $N_a$  is the number of atoms per unit area of the surface,  $A_a$  is a constant;  $d = d_a + d_A$ , where  $d_a$  is the diameter of an adsorbent atom, and  $d_A$  is the diameter of the adsorbate molecule. The condition  $l > d$  must be satisfied for the interaction model to remain valid.

A comprehensive analysis of LiFePO<sub>4</sub>'s textural properties as a cathode material was conducted using BET surface area measurements in conjunction with BJH and HK pore structure analyses (Figures 4 and 5, Table 1). The resulting data detailing specific surface area, PDS, and pore diameter profiles offer key insights into the structure property relationships governing the material's suitability for lithium-ion battery applications.

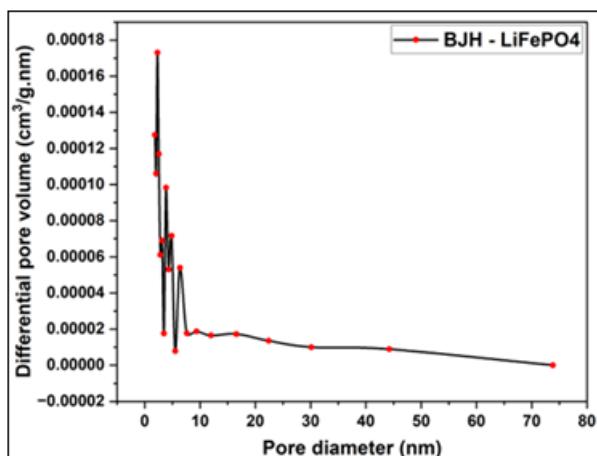


**Figure 4.** Variation of the differential pore volume ( $\text{cm}^3/\text{g}\cdot\text{nm}$ ) vs. pore diameter of the pore size distribution of LiFePO<sub>4</sub> using BJH method.

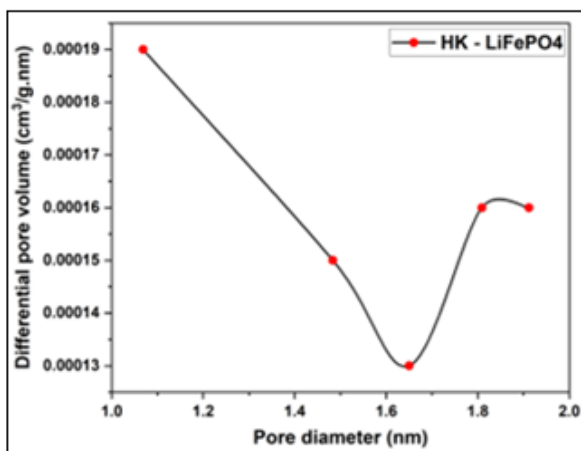


**Figure 5.** Variation of the differential pore volume ( $\text{cm}^3/\text{g}\cdot\text{nm}$ ) vs. pore diameter of the pore size distribution of synthesized LiFePO<sub>4</sub> using HK method.

**Table 1.** Specific surface area and pore characteristics of LiFePO<sub>4</sub> powder.

Sample	BET Surface Area (m <sup>2</sup> /g) (±2–5%)	Total Pore Volume (cm <sup>3</sup> /g) (±2–5%)	V <sub>micropore</sub> (cm <sup>3</sup> /g) (±2–5%)	V <sub>mesopore</sub> (cm <sup>3</sup> /g) (±2–5%)	Average Pore Diameter (nm) (±0.5 nm)
LiFePO <sub>4</sub>	1.2	1.4 × 10 <sup>-3</sup>	5 × 10 <sup>-4</sup>	9 × 10 <sup>-4</sup>	4.7

The results indicate that the LiFePO<sub>4</sub> powder possesses a low BET surface area of 1.2 m<sup>2</sup>/g and a limited total pore volume of 1.4 × 10<sup>-3</sup> cm<sup>3</sup>/g, with mesopores accounting for the majority (9 × 10<sup>-4</sup> cm<sup>3</sup>/g) and an average pore diameter of 4.7 nm above the 2 nm threshold that defines microporosity. This low pore volume suggests limited capacity for electrochemical reactions and restricted transport of lithium ions within the pristine LiFePO<sub>4</sub> structure. To mitigate these limitations, the incorporation of activated carbon as a conductive support is proposed. Activated carbon can significantly increase the surface area and porosity of the composite, thereby improving electrolyte–electrode contact and facilitating more efficient lithium-ion diffusion.

The pore size distribution derived using the BJH method, exhibits prominent peaks at approximately 2 nm, 4 nm, 6 nm, and 42 nm. This confirms that mesopores dominate the pore structure—an attribute favorable for enhancing lithium-ion diffusion and improving electrochemical performance.

### 3.2. Chemical and Physical Characterization of Activated Carbons at 700 °C from Millet Cob (MC) and Water Hyacinth (WH)

#### 3.2.1. BET Surface, Pore Size and Pore Distribution Determination of Activated Carbons at 700 °C from MC and WH

##### Adsorption and Desorption Isotherms of Activated Carbons from MC and WH

Figure 6a,b present, respectively, the nitrogen adsorption/desorption isotherms for activated carbons derived from MC and WH. These curves distinctly reveal the characteristic pore structures of each material, reflecting differences in surface area, pore volume, and distribution resulting from their respective activation and precursor properties.

These isotherm diagrams vary depending on the KOH-to-biomass mass ratios used during activation (KOH/MC 1:1, 2:1, and 5:1). For both MC and WH-derived activated carbons, a decreasing trend in maximum nitrogen uptake is observed with increasing KOH content. This behavior may reflect changes in pore structure and surface chemistry induced by the higher activating agent concentrations.

The nitrogen adsorption/desorption isotherms of functionalized carbon samples from MC (KOH/MC 1:1, 2:1, and 5:1) and WH (KOH/WH 1:1, 2:1, and 5:1) exhibit type IV profiles with H4-type hysteresis loops, indicative of a dominant mesoporous structure [50]. The isotherm curves can be interpreted in three distinct regions:

Region I ( $P/P_0 < 0.2$ ): The overlap of adsorption and desorption branches corresponds to monolayer adsorption, characteristic of micropore filling [51].

Region II ( $0.2 < P/P_0 < 0.5$ ): The initial divergence between the branches suggests the presence of partially developed pores and progressive multilayer formation within the micropore–mesopore transition region [38,52].

Region III ( $P/P_0 > 0.5$ ): A pronounced hysteresis loop appears, attributed to capillary condensation in open mesopores and larger macropores [38].

The presence of all three regions confirms a hierarchical pore system composed of micropores, mesopores, and macropores. This structural complexity is further supported by the pore size distribution data, which aligns with the trends observed in the isotherm profiles.

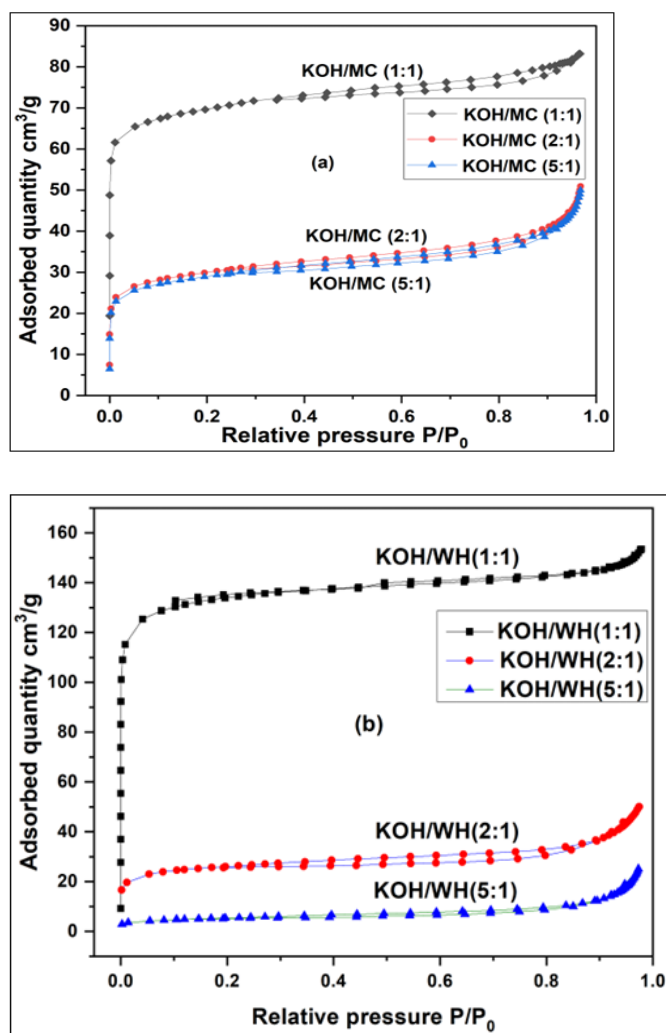


**Figure 6.** (a) Nitrogen adsorption / desorption isotherms of millet cob (MC) at the ratios KOH/MC of: KOH/MC= 1:1; KOH/MC =2:1; KOH/MC = 5:1; (b) Nitrogen adsorption/desorption isotherms of water hyacinth (WH) at the ratios KOH/WH of: KOH/WH= 1:1; KOH/WH =2:1; KOH/WH = 5:1.

#### Distribution of the Pore Dimensions of the Activated Carbons

Pore size distribution encompasses both micropores and mesopores, each contributing distinct functional advantages. Micropores offer a high specific surface area, thereby enhancing lithium-ion adsorption capacity, while mesopores facilitate more efficient lithium-ion diffusion within the cathode structure.

#### Case of the Water Hyacinth (WH) Sample

The micropore size distributions of WH-derived activated carbon samples, synthesized at different KOH/WH mass ratios, were estimated using the HK method and are shown in Figure 7a–c. Complementary analysis of mesopores and macropores was conducted using the NLDFT model, as presented in Figure 7d–f.

In Figure 7a, the HK method reveals a dominant micropore ( $D < 2$  nm) peak centered at 0.58 nm. A comparable result is obtained in Figure 7d using the NLDFT method, which shows a peak at approximately 0.50 nm, confirming consistency between the two models. For the samples corresponding to Figure 7b,c (KOH/WH 2:1 and 5:1), broader and weaker peaks are observed near 1.8 nm, indicating a shift in pore size distribution with increased activation ratio. These findings align with the NLDFT profiles in Figure 7e,f, where peaks appear at 1.65 nm, suggesting the presence of wider micropores or narrow mesopores.

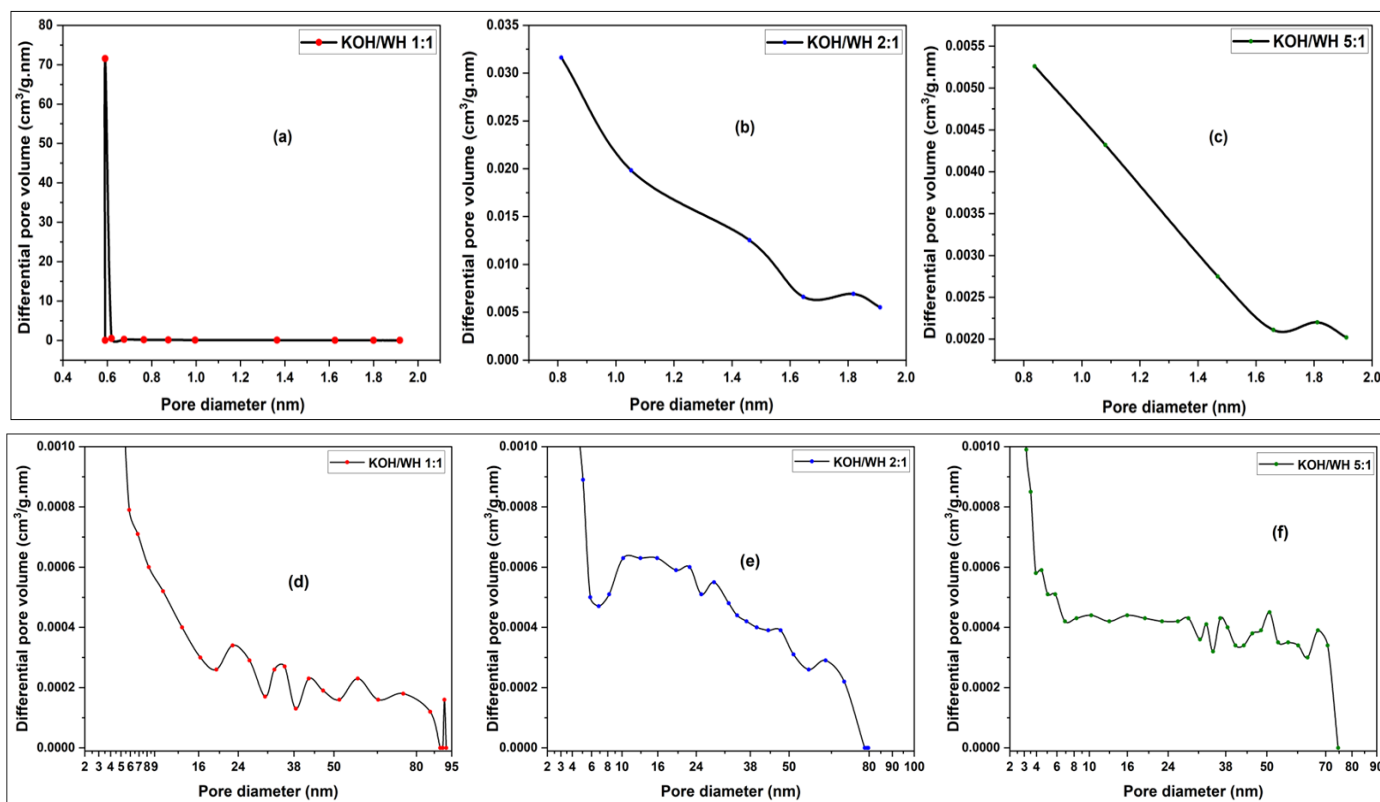


**Figure 7.** KOH/WH pore size distribution using HK method: (a) KOH/WH 1:1 (b) KOH/WH 2:1 and (c) KOH/WH 5:1 at 700 °C; KOH/WH pore size distribution using NLDFT method: (d) KOH/WH 1:1 (e) KOH/WH 2:1 and (f) KOH/WH 5:1 at 700 °C.

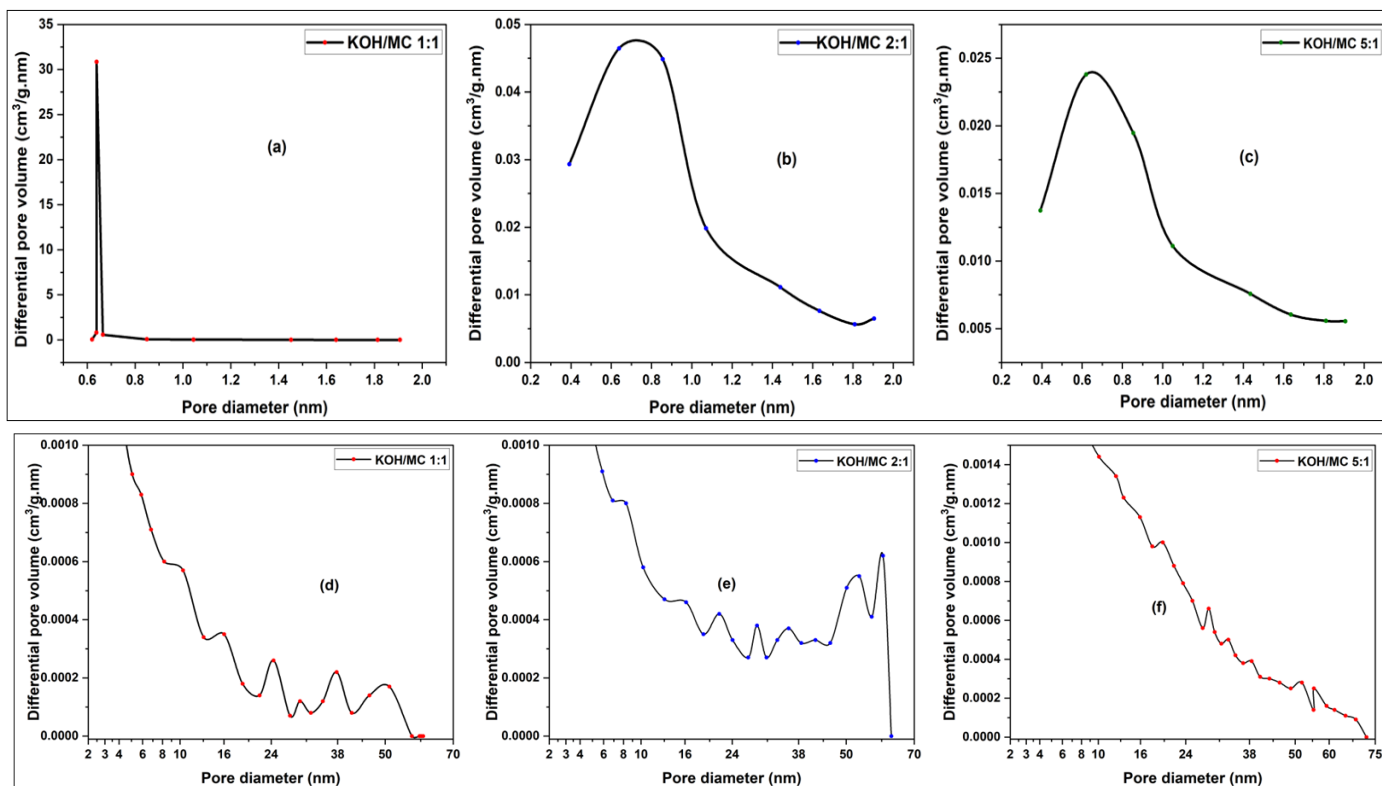
Notably, the micropore diameter for the KOH/WH 1:1 sample (0.58 nm) is at least three times smaller than those of the KOH/WH 2:1 and 5:1 sample (1.8 nm), highlighting the influence of activation intensity on pore development. This progressive shift in pore size distribution may directly impact on the electrochemical accessibility and ion transport behavior of the resulting carbon materials.

Figure 7d shows that the KOH/WH 1:1 sample exhibits mesopore peaks at 2.15, 5.1, 23, 35, and 42 nm, with additional macropore features at 58, 75, and 92 nm. In contrast, the KOH/WH 2:1 sample (Figure 7e) displays a broader mesopore distribution, with peaks at 2.15, 2.40, 2.83, 3.96, 10, 22, 28, and 47 nm, along with a single macropore peak at 63 nm. Similarly, the KOH/WH 5:1 sample (Figure 7f) reveals mesopores at 2.15, 2.55, 4.45, 5.82, 10.3, 16, 29, and 37 nm, accompanied by weak macropore ( $D > 50$  nm) signals at 51 and 67 nm. Across all samples, mesopores are more prevalent than macropores. Notably, the 2:1 and 5:1 sample exhibit a greater number and broader distribution of mesopores compared to the 1:1 sample, suggesting the development of a more complex and well-interconnected mesoporous network.

This richer mesopore architecture is expected to enhance electrolyte accessibility, as a broader range of mesopore sizes, within an optimal window facilitates more efficient lithium-ion diffusion in Li-ion battery systems. Furthermore, the improved mesopore distribution may promote better surface utilization, thereby increasing charge storage capacity. The presence of interconnected pores of varying sizes can also reduce ionic transport resistance by optimizing electrolyte penetration and ion flow pathways. Conversely, the KOH/WH 1:1 sample, characterized by fewer but larger mesopores, may favor bulk ion transport yet offer lower active surface area. The weak macropore signatures observed in all cases suggest that macropores contribute minimally to the electrochemical behavior of these materials.

### Case of the Millet cob (MC) sample

Figure 8a displays a prominent micropore peak centered at approximately 0.64 nm. A comparable result is observed in the NLDFT model (Figure 8d), where the micropore peak is located around 0.51 nm. Similarly, the HK model results shown in Figure 8b,c also exhibit dominant peaks near 0.64 nm, while the corresponding NLDFT profiles in Figure 8e,f confirm micropore sizes of approximately 0.5 nm. Unlike the WH-based samples, the micropore size of the MC-derived activated carbon remains largely unaffected by variations in the KOH/MC activation ratio. This indicates that, for this biomass precursor, the micropore dimensions are more dependent on the intrinsic structural characteristics of the raw material than on the activation intensity.



**Figure 8.** KOH/MC pore size distribution using HK method: (a) KOH/MC 1:1 (b) KOH/MC 2:1 and (c) KOH/MC 5:1 at 700 °C; KOH/MC pore size distribution using NLDFT method: (d) KOH/MC 1:1 (e) KOH/MC 2:1 and (f) KOH/MC 5:1 at 700 °C.

The pore structure of activated carbon derived from MC varies with the KOH/MC mass ratio. For the KOH/MC 1:1 sample (Figure 8d), mesopore peaks are observed at 2.28, 3.96, 16, 24.5, and 38 nm, along with a weak macropore feature at 52 nm. The KOH/MC 2:1 sample (Figure 8e) exhibits mesopores at 2.3, 3.94, 16.2, 21.7, 28.88, 35.72, and 42 nm, accompanied by minor macropore signals at 53.6 and 60.4 nm. In the KOH/MC 5:1 sample (Figure 8f, NLDFT model), mesopore ( $2 \text{ nm} < D < 50 \text{ nm}$ ) peaks occur at 2.40, 4.45, 19.75, 28.67, and 38.52 nm, with additional macropores detected at 52 and 55 nm.

The micropore size distribution remains largely consistent across all KOH/MC ratios, suggesting that micropore formation is relatively insensitive to activation intensity in MC-derived carbons. In contrast, mesopore characteristics are clearly influenced by the KOH ratio, with higher ratios generating broader and more complex mesopore distributions. Macropore size, however, remains relatively unchanged. This behavior contrasts with that of WH-derived samples, where micropore, mesopore, and macropore features all vary significantly with activation ratio.

### BET Surface Area of Functionalized Carbons from MC and at WH

Table 2 summarizes the key textural properties of all activated carbon samples, including BET surface area, total pore volume, micropore volume, mesopore volume, and average pore diameter. For both WH and MC-derived carbons, an increase in the KOH activation ratio leads to two consistent trends: (1) a reduction in BET surface area and total pore volume, and (2) an increase in average pore diameter. This shift toward larger pore sizes is primarily attributed to a decrease in micropore volume, indicating that more intensive chemical activation promotes pore expansion at the expense of microporosity.

**Table 2.** Surface parameters of activated carbons from MC and WH at 700 °C.

Sample	BET Surface Area (m <sup>2</sup> /g) (±2–5%)	Total Pore Volume (10 <sup>-3</sup> cm <sup>3</sup> /g) (±2–5%)	V <sub>micropore</sub> (10 <sup>-3</sup> cm <sup>3</sup> /g) (±2–5%)	V <sub>mesopore</sub> (10 <sup>-3</sup> cm <sup>3</sup> /g) (±2–5%)	Average Pore Diameter (nm) (±0.5 nm)
KOH/WH 1:1	413.0	237.6	203.1	34.3	2.3
KOH/WH 2:1	83.2	77.4	39.1	38.2	3.7
KOH/WH 5:1	18.53	38.9	7.5	12.9	8.4
KOH/MC 1:1	216.3	128.6	104.3	24.3	2.4
KOH/MC 2:1	95.8	78.7	46.9	31.1	3.3
KOH/MC 5:1	57.8	76.3	28.0	48.0	5.3
Graphite	45.1	75	21	53	6.6

The observed reduction in BET surface area for both MC and WH-derived activated carbon samples at higher KOH activation ratios can be attributed to two primary mechanisms. First, excessive KOH concentrations may promote excessive pore widening during chemical activation, resulting in a decline in micropore density and, consequently, a lower overall surface area. Second, the formation and retention of residual KOH or potassium-containing byproducts may lead to partial pore blockage, further limiting surface accessibility. These structural alterations, particularly the loss of microporosity and potential occlusion of diffusion pathway, may adversely affect the electrochemical performance of Li-ion batteries by reducing lithium-ion accessibility.

#### 3.2.2. SEM Characterization of Activated Carbons at 460 °C and 700 °C from Millet Cob and Water Hyacinth

SEM analysis of samples carbonized at 460 °C (KOH/MC and KOH/WH 2:1) (Figure 9) revealed irregular, blocky morphologies with large pore sizes of approximately 2600 nm and 1600 nm, and no evidence of mesopores or micropores. These structures, indicative of incomplete carbonization, are further corroborated by the low carbon content (~30 wt%) measured in these samples (see Section 3.2.3). Due to their poorly developed porosity and limited carbon content, these materials are not suitable for use as electrode components in Li-ion battery systems.

In contrast, SEM micrographs of activated carbons synthesized at 700 °C (Figure 10) exhibit well-developed, homogeneous porous morphologies across all KOH/MC and KOH/WH mass ratios. The elevated carbonization temperature promotes complete thermal decomposition and efficient chemical activation by KOH, leading to structurally robust carbon matrices with high carbon content ( $\geq 85$  wt%; see Section 3.2.3). At this temperature, the evolution of volatile species and enhanced etching reactions facilitate the generation of interconnected pore networks unique to each activation condition.

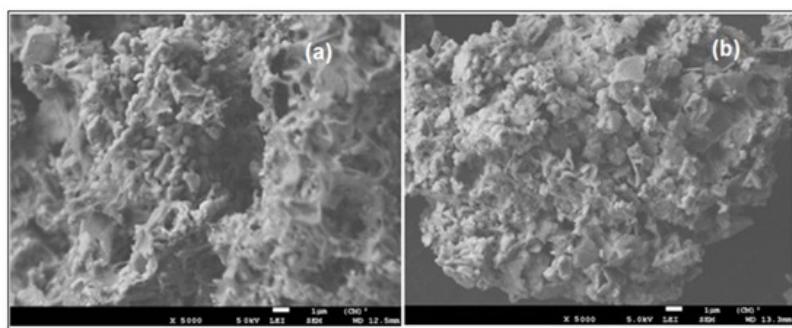


**Figure 9.** SEM images of millet cob activated carbon at 460 °C: (a) KOH/MC 2:1; (b) KOH/WH 2:1.

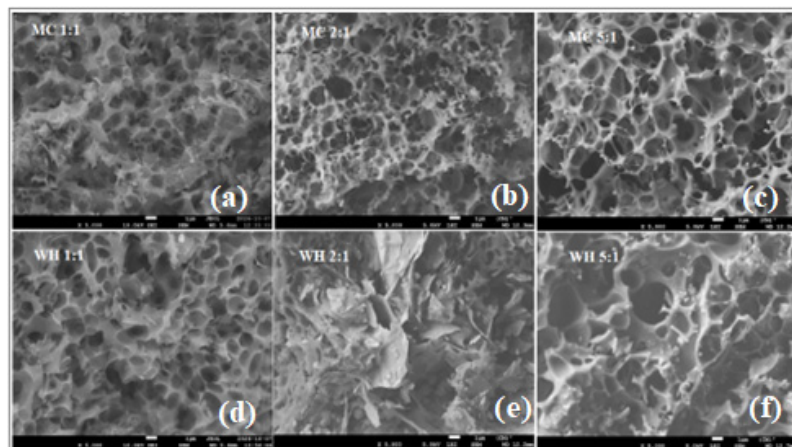


**Figure 10.** SEM images of various activated carbon at 700 °C: (a) KOH/MC 1:1; (b) KOH/MC 2:1; (c) KOH/MC 5:1; (d) KOH/WH 1:1; (e) KOH/WH 2:1; (f) KOH/WH 5:1.

Samples prepared with lower KOH concentrations (KOH/MC and KOH/WH 1:1) display a high density of small, uniform pores. This is attributed to the moderate reactivity of KOH at this ratio, which limits excessive carbon wall degradation while favoring the development of fine porosity. As illustrated in Figure 10a,d, these pore structures are advantageous for applications requiring high surface area, particularly in energy storage systems where micropore presence plays an important role in enhancing adsorption capacity and lithium-ion storage performance.

Samples activated with higher KOH ratios (KOH/MC and KOH/WH 2:1 and 5:1) exhibit increased pore sizes compared to those prepared at a KOH 1:1 ratio. Notably, the KOH/WH 2:1 sample reveals a graphite-like layered morphology, in which the interlayer spacing forms a porous network that may facilitate lithium-ion diffusion. For both biomass at the KOH ratio 5:1, the pore structures (Figure 10c,f) appear more open and less compact, suggesting that excessive KOH concentrations can lead to partial degradation of the carbon framework—enlarging pore size while diminishing pore density and potentially reducing the specific surface area.

While higher KOH content enhances chemical activation by promoting the removal of volatile matter and increasing porosity, the 2:1 ratio appears to strike a balance between pore development and structural integrity—making it the most favorable condition for Li-ion battery applications among the studied ratios. In contrast, further increasing the KOH ratio to 5:1 induces structural collapse, resulting in fewer, oversized pores that may hinder electrochemical performance.

These observations underscore the necessity of optimizing both the KOH/carbon ratio and carbonization temperature (with 700 °C proving effective) to tailor the porosity of biomass-derived carbons for energy storage. The KOH/WH 2:1 sample carbonized at

700 °C demonstrates a particularly promising pore architecture, aligning well with the structural and functional demands of lithium-ion battery electrodes.

### 3.2.3. Elemental Composition of Porous Carbons from MC and WH Using EDS

Table 3 presents the EDS results for samples activated at 460 °C with a KOH/carbon 2:1 ratio. The carbon content in both samples does not exceed 30 wt%, indicating incomplete carbonization of the organic precursors. Additionally, the EDS profiles reveal higher relative concentrations of oxygen and potassium compared to carbon, further supporting the presence of residual activating agents and unconverted biomass. These findings confirm insufficient thermal decomposition at this activation temperature.

**Table 3.** Chemical composition (%mass with an error range of 0.1–0.5%) using EDS of activated carbon from MC and WH at 460 °C.

Samples	KOH/CM	C (%)	O (%)	K (%)	Na (%)	Cl (%)	Al (%)	Si (%)	Mg (%)	P (%)
MC 460 °C	2:1	30	33	35	-	-	0.2	1.7	0.1	-
WH 460 °C	2:1	26	41	30	0.3	1.4	0.1	0.4	0.3	0.1

Table 4 summarizes the EDS results of activated carbon samples derived from various KOH/carbon mass ratios, all carbonized at 700 °C. Compared to those carbonized at 460 °C, these samples consistently show carbon contents exceeding 70 wt%, indicating successful carbonization at elevated temperatures. The data also reveal a systematic decrease in carbon content with increasing KOH ratios. For MC-derived samples, the carbon content decreases from 85.5% at KOH/MC 1:1 to 71% both KOH/MC 2:1 and 5:1. Similarly, for water hyacinth-based samples, carbon content declines from 80% (KOH/WH 1:1) to 70% (KOH/WH 2:1 or 5:1).

**Table 4.** Chemical Composition using EDS Activated Carbon from MC and WH at 700 °C.

Samples	KOH/C	Chemical Elements (% Mass with an Error Range of 0.1–0.5%)											
		C	O	K	Na	Cl	Al	Si	Fe	Ca	Mg	S	P
Millet cob	1:1	85.5	12	2	-	0.3	-	0.2	-	-	-	-	-
	2:1	71.5	19	6	0.1	0.8	0.8	1.1	0.1	0.1	0.1	0.4	-
	5:1	71.0	20	8.3	-	0.1	0.2	0.3	-	-	-	0.1	-
Water hyacinth	1:1	80.0	13	2	-	2	0.2	0.5	0.4	0.8	0.1	0.9	0.1
	2:1	70.0	18	8	0.1	1.8	0.2	0.7	0.1	0.6	0.2	0.2	0.1
	5:1	70.0	18	8	0.1	2.4	0.1	0.4	0.2	0.2	0.1	0.5	-

This reduction in carbon content is attributed to intensified chemical activation at higher KOH concentrations, which promotes gasification reactions that convert carbon into CO<sub>2</sub> or potassium-based compounds such as K<sub>2</sub>CO<sub>3</sub>. The resulting loss of carbon during activation leads to lower carbon yields in the final product. Additionally, the increasing levels of oxygen and potassium detected in samples with higher KOH/carbon ratios reflect the retention of potassium species—either as residual unreacted KOH or as activation byproducts such as potassium carbonates.

The observed increase in oxygen content from 12% to 20% for MC and from 13% to 18% for WH indicates an accumulation of oxygenated functional groups and oxygen-containing inorganic residues (e.g., carbonates). Similarly, the potassium content rises significantly, from 2% to 8.3% for MC and from 2% to 8% for WH, likely due to the formation

of potassium-based compounds such as  $K_2CO_3$  and  $K_2O$ . These species may become embedded within the porous carbon matrix, particularly at elevated KOH concentrations.

Increasing the KOH/MC or KOH/WH mass ratio intensifies the activation process, promoting the development of larger pores and a more open structure. However, excessive KOH can also trigger gasification reactions that convert a portion of the carbon into gaseous by-products, thereby reducing carbon yield and introducing additional potassium residues. The concurrent rise in oxygen content suggests the persistence of residual oxygen-containing functional groups, further reflecting incomplete carbonization or the retention of oxidized species.

### 3.2.4. X-Ray Diffraction Studies of Porous Carbons from Millet Cob and Water Hyacinth

Figure 11 presents the XRD patterns of activated carbon samples prepared from millet cob (KOH/MC 2:1) and water hyacinth (KOH/WH 2:1) at an activation temperature of 460 °C. Both patterns exhibit distinct crystalline reflections, suggesting the presence of ordered structural components. However, the observed peaks do not correspond to that characteristic of typical carbonaceous phases such as graphite or crystallin/amorphous carbon. Instead, the diffraction features are likely associated with residual inorganic species originating from the activating agent (KOH) or undecomposed mineral constituents intrinsic to the biomass precursors. These results indicate that at 460 °C, the activation temperature is insufficient to achieve complete carbonization and removal of non-carbonaceous phases.

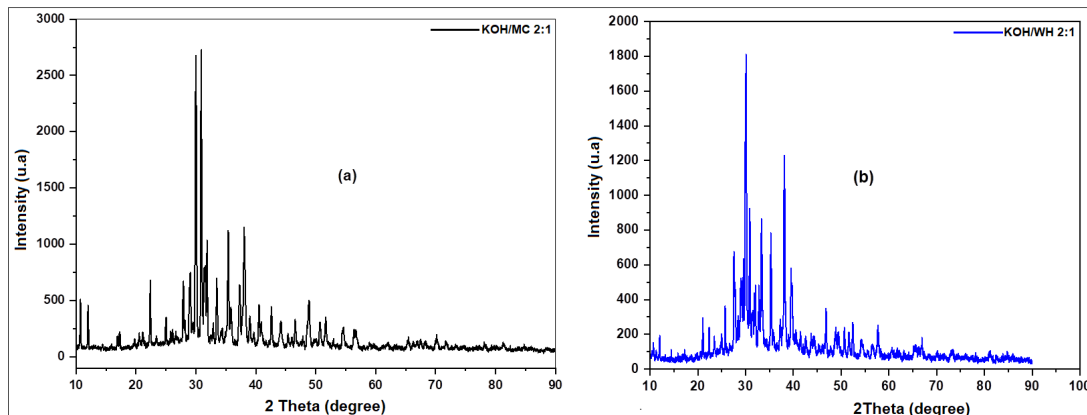


**Figure 11.** XRD patterns of activated carbon samples prepared from millet cob (KOH/MC 2:1) (a) and water hyacinth (KOH/WH 2:1) (b) at an activation temperature of 460 °C. Both patterns exhibit distinct crystalline reflections, suggesting the presence of ordered structural components.

The very low intensity of diffraction features attributable to carbonaceous phases suggest that the more prominent sharp peaks in the XRD patterns may arise from crystalline inorganic contaminants. This interpretation is supported by the EDS data presented in Table 3, which indicate the presence of silicon in the activated carbon—1.7 wt% for MC-derived samples and 0.4 wt% for WH-derived samples. The absence of well-defined carbon peaks further implies that carbonization and chemical activation were incomplete at 460 °C. This insufficient thermal treatment likely resulted in the retention of residual inorganic species originating from the precursor biomass and the activating agent (KOH), including metal oxides, potassium salts, or other processing-related impurities [53]. The low carbon content detected via EDS in these samples further corroborates the predominance of non-carbonaceous components.

Figure 12 presents the XRD patterns of activated carbon samples synthesized at 700 °C for KOH/carbon mass ratios of 1:1, 2:1, and 5:1, alongside the reference pattern for pure graphite (PDF 00-056-0159). Activation at this elevated temperature enhances the decom-

position of organic constituents and facilitates the development of a more ordered and graphitized carbon matrix, as evidenced by the emergence of broader yet distinguishable carbon diffraction peaks.

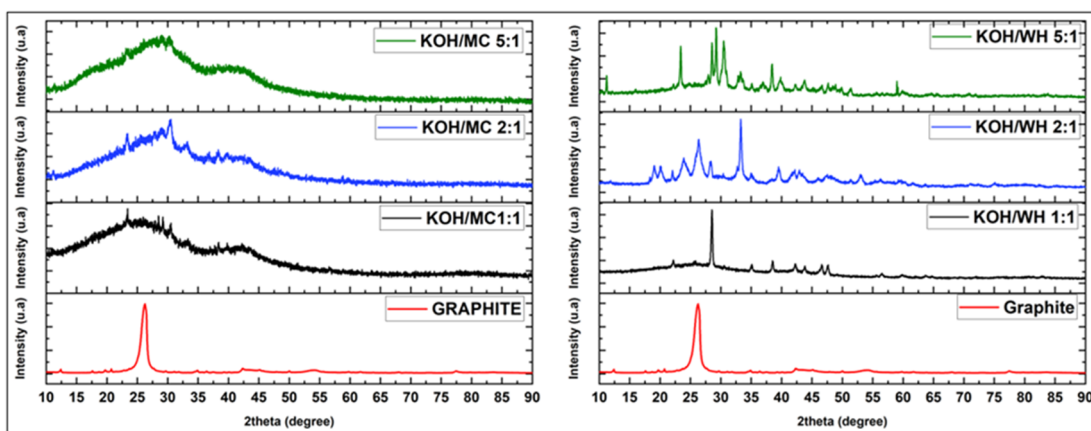


**Figure 12.** XRD patterns of activated carbon at 700 °C from Millet Cob (MC): KOH/MC 1:1, KOH/MC 2:1, KOH/MC 5:1, pure graphite and from Water Hyacinth: KOH/WH 1:1, KOH/WH 2:1, KOH/WH 5:1, pure graphite (this work).

The XRD patterns of KOH-activated carbon samples derived from MC (KOH/MC 1:1, 2:1, and 5:1) exhibit two broad diffraction features: a more intense peak centered around  $2\theta = 26^\circ$  and a weaker one at  $2\theta = 43^\circ$ . The broadness of these peaks and the absence of sharp reflections confirm the predominantly amorphous nature of the carbonaceous framework, which is characteristic of chemically activated carbon materials [54–57]. The peak at  $2\theta = 26^\circ$  is attributed to the (002) diffraction plane, while the signal at  $2\theta = 43^\circ$  corresponds to the (100) plane, both typically associated with graphitic carbon structures [54,56,58–60]. The XRD patterns of pure graphite in this work (Figure 12) are in agreement of the results obtained elsewhere on this material [61]. EDS analysis supports this structural characterization, revealing decreasing carbon contents of 85.5 wt% (1:1), 71.5 wt% (2:1), and 71 wt% (5:1). However, for the 1:1 and 2:1 sample, the presence of weak sharp peaks superimposed on the broad humps suggests a minor crystalline phase embedded within the largely amorphous matrix, potentially arising from residual inorganic species or structural impurities.

A comparative analysis of the three MC-derived samples shows a gradual decrease in crystallinity with an increasing KOH ratio, indicating a transition toward a more disordered structure. Quantitative crystallinity indices reveal a decline from 12.7% (KOH/MC 1:1) to 11.9% (KOH/MC 2:1), and down to 8.6% (KOH/MC 5:1), underscoring the impact of elevated KOH concentrations disrupting graphitic domains. This degradation is attributed to intensified chemical etching by KOH, which generates porosity at the expense of crystalline order by disintegrating graphitic planes.

In contrast, XRD patterns of WH-derived activated carbon (Figure 12) exhibit features of more crystalline carbon across all mass ratios (KOH/WH 1:1, 2:1, and 5:1). Each sample displays a sharp peak at  $2\theta = 26^\circ$ , corresponding to the (002) plane of graphitic carbon as indexed in PDF reference 00-056-0159, alongside a second sharp peak at  $2\theta = 43^\circ$ , attributed to the (111) plane of carbon (PDF 00-060-0053).

These patterns reveal a strong dependency of crystallinity on the KOH/WH ratio. The intensity of both graphite-associated peaks increases from KOH/WH 1:1 to 2:1, with a slight decline observed at 5:1. Quantitative analysis of crystallinity confirms this trend, with values rising from 40.5% (1:1) to 51.8% (2:1), before decreasing slightly to 50.6% (5:1). These results suggest that while moderate KOH concentrations enhance graphitic domain development, excessive activation may disrupt structural order.

Additional sharp peaks observed in the XRD patterns for all KOH/WH samples are attributed to residual inorganic elements—such as potassium (K), sodium (Na), iron (Fe), and chlorine (Cl)—which are known as byproducts of incomplete rinsing or activation residue [53]. EDS analysis corroborates their presence, indicating that these extraneous species influence diffraction behavior and reflect the imperfect removal of chemical by-products during the post-activation washing process [53].

### 3.2.5. Electric Conductivity of Activated Carbons from MC and WH

The fabrication of carbon platelets from powdered activated carbon using a hydraulic press reveals that electrical conductivity is sensitive to the applied pressure during compression [62]. Additionally, morphological characteristics and pore distribution are known to significantly influence electrical conductivity in porous carbons [63,64]. To ensure consistency and eliminate pressure-induced variability, all platelets were produced under identical conditions: a uniaxial pressure of 600 kPa and constant sample mass for each type of activated carbon.

Electrical conductivity measurements indicate that samples derived from MC and WH, activated at 460 °C, exhibit negligible conductivity. This result is consistent with insufficient carbonization at this lower activation temperature. In contrast, samples activated at 700 °C demonstrate markedly improved conductivity, as presented in Table 5.

**Table 5.** Evolution of electrical conductivity as a function of the mixing ratio of potassium hydroxide and activated carbon materials KOH/CM: CM= Carbon Materials.

Sample	Mixing Ration (KOH/CM)	Electrical Conductivity ( $10^{-3}$ S·cm $^{-1}$ ) ( $\pm 0.5\text{--}1.5\%$ )	Total Pore Volume ( $10^{-3}$ cm $^3$ /g) ( $\pm 2\text{--}5\%$ )	Average Pore Diameter (nm) ( $\pm 0.5$ )
Graphite	Reference	672	75	6.6
	1:1	6.74	237.60	2.30
Millet cob	2:1	8.42	77.40	3.72
	5:1	4.99	38.90	8.38
	1:1	8.92	128.60	2.38
Water hyacinth	2:1	14.70	78.70	3.29
	5:1	6.40	76.30	5.28

The electrical conductivity of both MC and WH-derived activated carbon samples vary as a function of the KOH/carbon mass ratio. The highest conductivity for each biomass type is observed at a KOH/CM 2:1 ratio, with the KOH/WH 2:1 sample exhibiting a significantly higher conductivity value ( $1.47 \times 10^{-2}$  S·cm $^{-1}$ ) compared to KOH/MC 2:1 ( $8.42 \times 10^{-3}$  S·cm $^{-1}$ ). Additionally, the samples prepared with a 1:1 mass ratio (KOH/MC 1:1 and KOH/WH 1:1) show higher conductivity than their 5:1 counterpart. These results suggest that electrical conductivity is maximized in samples with moderate total pore volumes, and equilibrium in micro/mesopore as reported in Table 5 for the KOH/WH 2:1 sample. Conversely, the formation of overly large pores in the KOH/WH 5:1 sample appears to impede conductivity, likely due to a reduction in the density of effective conductive pathways within the carbon matrix. This is attributed to the need of electrons to travel through carbon materials with large pores on longer distances which increases the electric resistance. Distances. In comparison, moderate total pore volume creates small pathways which allow fast electrons transfer, leading to higher conductivity.

The commercial graphite exhibited more high conductivity than the activated bio-resources carbons. This might be due to differences in crystal structures (graphite is more

crystal-like structure than activated bio-resources carbons and/or the difference in surface treatment. The commercial graphite surface was already treated by oxidation and by fluorination to improve its electrochemical performance [65]. These findings indicate that specific surface area alone may not be the most reliable probe of the variation in the electrical conductivity. As reported in [66], electrical resistivity may increase with the surface area. But excessive pore enlargement—arising from the transformation of micropores into meso- and macropores—can diminish conductivity by disrupting the continuity of the conductive network [66,67]. The optimised pore size between 3 and 4 nm may help in this improvement of the conductivity. Accordingly, the reduced conductivity observed in the highly activated KOH/MC 5:1 and KOH/WH 5:1 sample could be attributed to the decreases of carbon content, nonconductive activation by-products and / or the increased degree of activation.

Overall, WH-derived samples consistently outperform MC-derived ones in electrical conductivity. As illustrated in Figure 12, this behavior is likely linked to the higher crystallinity of WH-based carbons, as evidenced by their more pronounced graphitic peaks in the XRD patterns. This observation is consistent with the findings of [68], which report enhanced electrical performance in carbonaceous materials possessing well-ordered graphite-like structures. Finally, KOH/CM 2:1 appears optimal for both precursors, striking a balance between pore development and retention of conductive domains, and thereby enabling superior electrical conductivity.

### 3.3. Electrochemical Characterization

#### 3.3.1. Specific Capacity of Anodes Based on Synthesized Activated Carbon

Figure 13 presents the charge/discharge profiles of the anodes based on MC and WH activated and Figure 14 displays the corresponding electrochemical curves of a commercial graphite (reference) electrode under identical conditions. The intersection points between the charge and discharge curves were used to determine the specific capacity (mAh/g) of each sample, as summarized in Table 6.

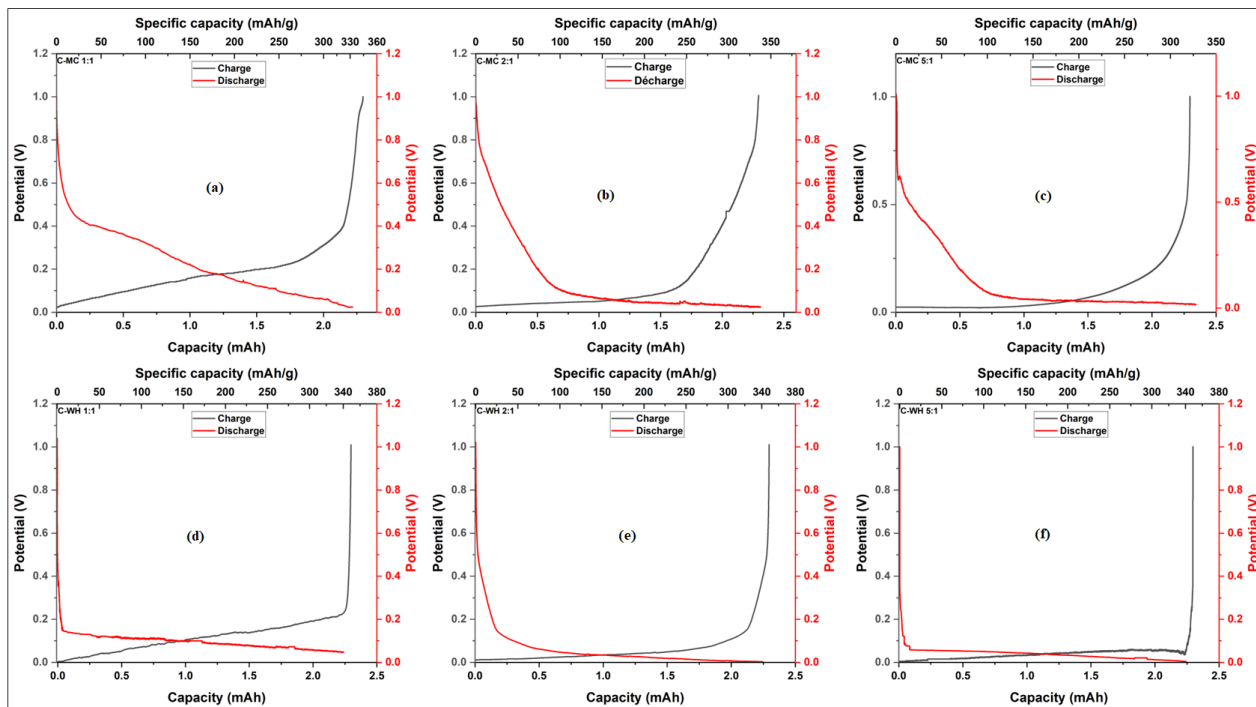


**Figure 13.** Charge/discharge at C/24, of Li-ion anodes based on KOH/MC 1:1 (a), 2:1 (b), 5:1 (c) and KOH/WH 1:1 (d), 2:1 (e), 5:1 (f).

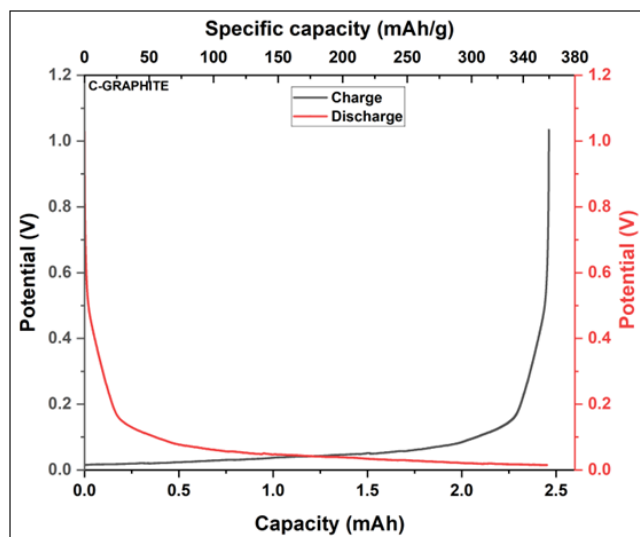


**Figure 14.** Charge/discharge (Li-ion anode based on commercial Graphite) at C/24.

**Table 6.** Respective specific capacity (mAh/g), anodes based on activated carbons based on Millet Cob (MC) and Water Hyacinth (WH) obtained from different ratios of KOH/CM and KOH/WH for a current rate of C/24.

Mixing Ratio (KOH/MC or KOH/WH) ( $\pm 2$ mAh/g)	Mixing Ratio (KOH/MC or KOH/WH) ( $\pm 2$ mAh/g)	Mixing Ratio (KOH/MC or KOH/WH) ( $\pm 2$ mAh/g)
Ok. Fine. No bolt also	1.1	2:1
Carbon of Millet cob	333	335
Water hyacinth	336	339

For comparison, the specific capacity obtained for commercial graphite based anode under C/24 cycling conditions, as shown in Figure 14, is  $362 \text{ mAh}\cdot\text{g}^{-1}$ , which closely aligns with the widely reported theoretical literature value of  $372 \text{ mAh/g}$  corresponding to the  $\text{LiC}_6$  anode [69]. This high value of the specific capacity of graphite is agreement with his high conductivity, optimized total pore volume and the diameter size. The specific capacities of the various activated carbon samples vary only slightly, ranging from a minimum of  $330 \text{ mAh}\cdot\text{g}^{-1}$  for the KOH/MC 5:1 sample (Figure 15c) to a maximum of  $339 \text{ mAh}\cdot\text{g}^{-1}$  for the KOH/WH 2:1 sample (Figure 13e). No substantial difference in specific capacity is observed between samples derived from millet cob and water hyacinth, or across different activation ratios.

According to the data presented in Table 6, samples prepared with KOH/carbon mass ratios of 1:1 and 5:1 exhibit marginally lower capacities, which is likely attributable to differences in pore architecture. Although micropores contribute significantly to the overall specific surface area, an excess of ultra-micropores ( $< 2 \text{ nm}$ ) can hinder lithium-ion penetration, imposing diffusion limitations. In contrast, a reasonable higher proportion of mesopores facilitates improved ion accessibility, enabling more efficient lithium-ion transport and deeper intercalation into the carbon structure.

The determination of the specific capacity of anodes based on new active carbons is important for carbon-based Li-ions batteries development because it is the limiting factor of the anode specific capacity.

The development of additive carbons with optimized parameters may play an important role in obtaining the best electrochemical performance of electrodes based on  $\text{LiFePO}_4$ /biomass-derived activated carbons.

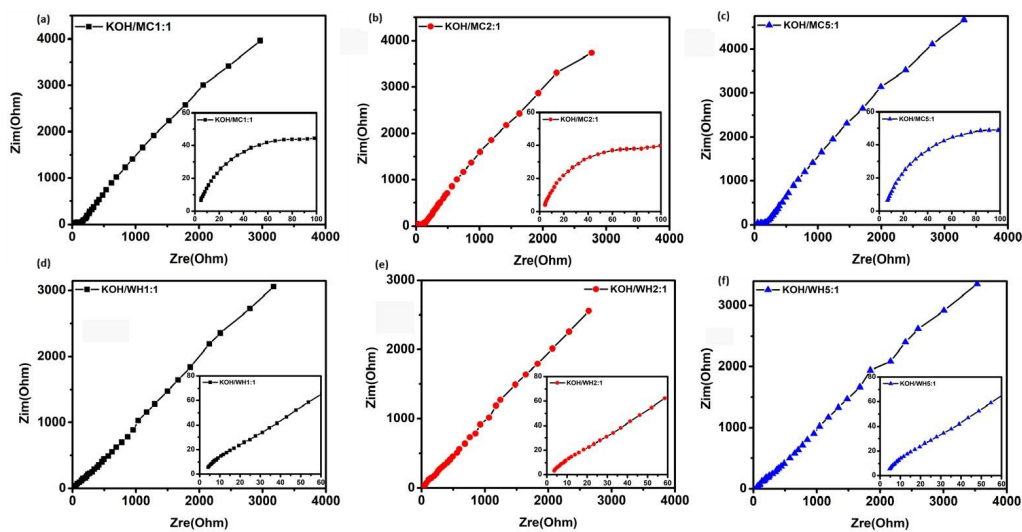


**Figure 15.** Nyquist diagram of EIS of anodes based on MC (a–c) and WH (d–f) carbon.

### 3.3.2. EIS Study of Synthesized Activated Carbon

To assess the battery characteristics based on the synthesized activated carbons, EIS measurements were conducted using Li/C half-cells. In this configuration, the cathode consisted of activated carbon coated onto an aluminum current collector, the anode comprised lithium metal, and the electrolyte was a solution of lithium hexafluorophosphate ( $\text{LiPF}_6$ ). Impedance spectra were recorded over a frequency range from 100 kHz to 0.1 Hz with a root mean square (RMS) amplitude of 5 mV. Measurements were benchmarked against those obtained from a standard Li/graphite half-cell. A Solartron 1255B frequency response analyzer coupled with a 273A potentiostat was employed for EIS acquisition.

The resulting Nyquist plots, along with their equivalent circuit models generated using ZSimpWin software, version 3.6, are presented in Figure 15 for activated carbon samples derived from MC (a, b, c) and WH (d, e, f). Activated carbon samples of KOH/CM 2:1 ratio, derived from both MC and WH, exhibit the most favorable electrochemical parameters, characterized by significantly lower  $R_{\text{ct}}$  compared to other samples. Samples synthesized at a KOH/CM 1:1 ratio rank next in performance, while those prepared at a KOH/CM 5:1 ratio show the highest  $R_{\text{ct}}$  values, indicating less favorable electrochemical behavior.

These trends are consistent with prior findings, where a combination of moderately enhanced crystallinity, optimized micro- and mesoporous structure, and elevated electrical conductivity synergistically contribute to improved impedance characteristics. The KOH/CM 2:1 sample, in particular, benefits from a balanced pore architecture and preserved graphitic domains, which collectively facilitate efficient charge transport and reduced interfacial resistance.

### 3.3.3. Analysis of the Electrochemical Characteristics of $\text{LiFePO}_4/\text{C}$ Electrode Study of Coulombic Efficiency

Coulombic efficiency, defined as the ratio of discharge capacity to charge capacity, is a metric for assessing electrochemical reversibility. Table 7 summarizes the Coulombic efficiency values for  $\text{LiFePO}_4/\text{C}$  half-cells. The LFP/MC 1:1, 2:1, and 5:1 configuration exhibit first-cycle. Similarly, the LFP/WH 1:1, 2:1, and 5:1 cell achieves efficiencies near 96%, with the LFP/WH 2:1 sample presenting slightly higher values compared to the others in the MC series.

**Table 7.** Coulombic efficiency in % of the first three cycles of the LiFePO<sub>4</sub>/C based cell.

Samples	Coulombic Efficiency (%) ± 1%			
	Cycle 1	Cycle 2	Cycle 3	Cycle 4
LFP/MC 1:1	95.0	100	99.8	99.6
LFP/MC 2:1	95.9	100	99.8	99.6
LFP/MC 5:1	95.5	100	99.7	99.5
LFP/WH 1:1	96.0	100	99.9	99.7
LFP/WH 2:1	96.4	100	100	99.9
LFP/WH 5:1	95.9	100	99.8	99.6

The improvement in Coulombic efficiency observed during the second cycle is indicative of the formation of a solid electrolyte interphase (SEI) at the electrode/electrolyte interface. This nanometric layer forms on the surface of the anode during the initial charge/discharge cycles of Li-ion batteries and results from the reaction between lithium ions and electrolyte components [70]. During the first charge cycle, a portion of lithium ions is irreversibly consumed to form this passivating layer, which explains why the initial capacity is not representative of the battery's true reversible capacity in subsequent cycles [71]. To investigate SEI formation and evaluate Coulombic efficiency, the cells were cycled at a C/12 rate for three cycles. A high Coulombic efficiency reflects minimal parasitic side reactions and efficient lithium-ion cycling [72]. Once the SEI stabilizes, subsequent cycles demonstrate improved charge retention, highlighting enhanced electrode–electrolyte compatibility and reduced side reactions [72,73]. While the first-cycle SEI formation dominates, long-term growth contributes to additional lithium and electrolyte consumption, ultimately degrading cell conductivity, capacity, and Coulombic efficiency over time [73,74]. This might be the reason why after cycle 2, the current efficiency is going slightly down as shown for cycle 3 and cycle 4 (Table 7).

#### Study of the Discharge of LiFePO<sub>4</sub> (LFP)/C at Different Current Rates

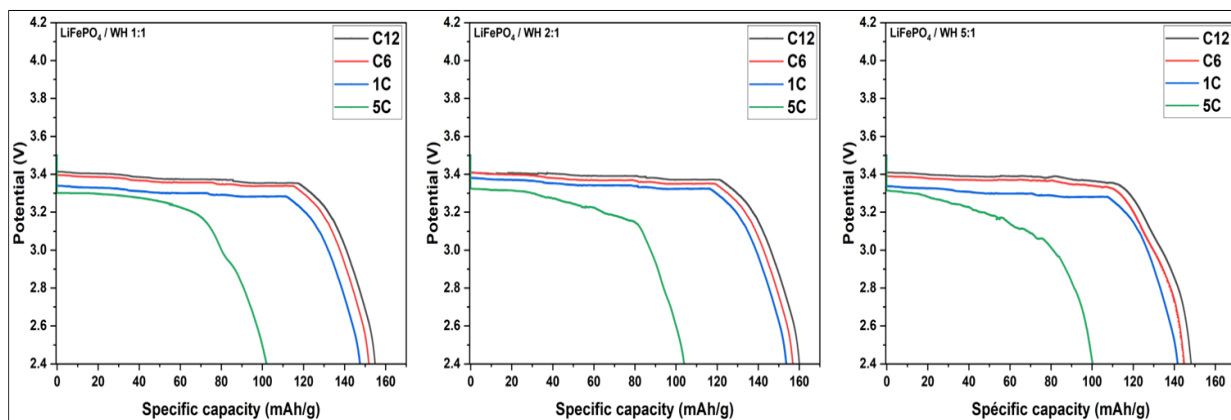
Using Lithium metal as the anode, the charge/discharge performance of LFP/C (MC, WH) cathodes was conducted at various current rates C/12, C/6, 1C, and 5C to assess the rate capability and overall electrochemical behavior of the composite electrodes under different operating conditions. The constant cycling current at each applied rate is calculated based on the active mass of the cathode, the C-rate current value, and the theoretical specific capacity of LFP (170 mAh/g).

The corresponding discharge profiles, presented in the respective figures, illustrate the reversibility and rate-dependent behavior of the electrodes. Figures 16 and 17 depict the discharge curves for LFP/C cathodes incorporating, respectively, an additive of 8% mass of MC-derived activated carbon at KOH/MC or KOH/WH, mass ratios of 1:1, 2:1, and 5:1.

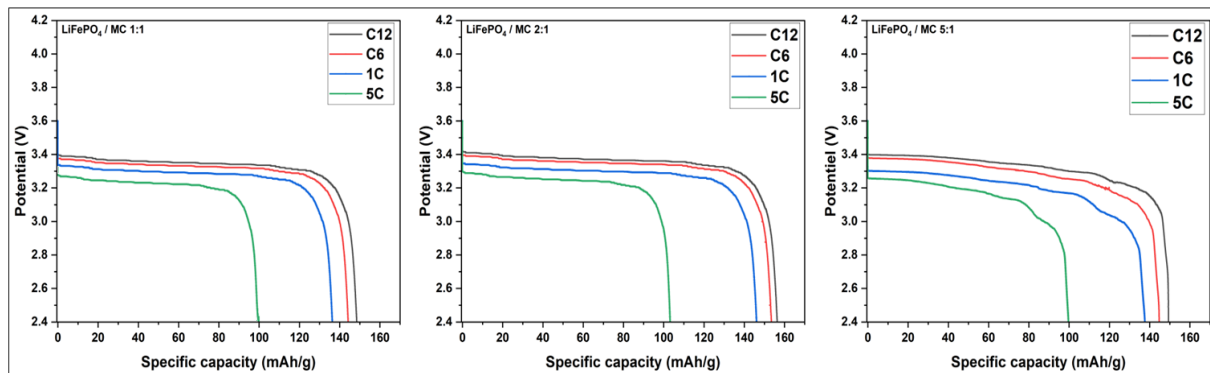
Figure 16 shows discharge curves at different current rates for LFP/C samples from millet cob. All samples display a well-defined voltage plateau near 3.4 V, characteristic of the Fe<sup>3+</sup>/Fe<sup>2+</sup> redox transition and associated with the biphasic reaction between FePO<sub>4</sub> and LiFePO<sub>4</sub>.

Figure 17 presents the discharge profiles of LiFePO<sub>4</sub>/C (WH) cathodes with samples KOH/WH1:1, 2:1, and 5:1. All samples also display a well-defined voltage plateau near 3.4 V, characteristic of the Fe<sup>3+</sup>/Fe<sup>2+</sup> redox transition and associated with the biphasic reaction between FePO<sub>4</sub> and LiFePO<sub>4</sub>. This behavior closely agrees with those observed for MC-derived carbon cathode.

Figure 18 shows the discharge curves for LFP with 8% mass of graphite. These curves exhibit a well-defined voltage plateau at 3.4 V, corresponding to the  $\text{Fe}^{3+}/\text{Fe}^{2+}$  redox couple and characteristic of the biphasic transition between  $\text{FePO}_4$  and LFP [75].



**Figure 16.** Discharge curves at different current rates for LFP/C samples from millet cob.



**Figure 17.** Discharge curves at different current rates for LFP/C samples from water hyacinth.

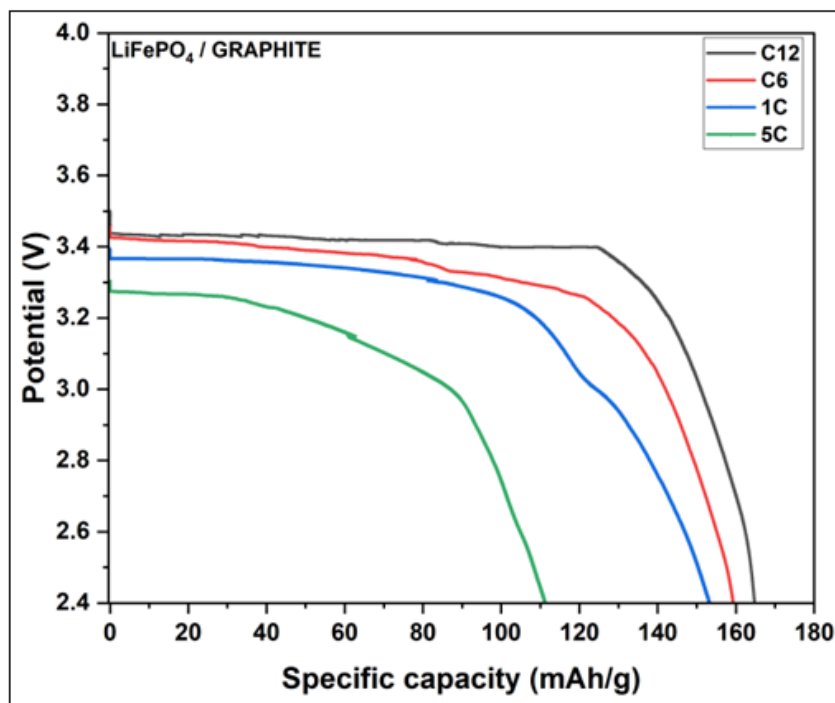


**Figure 18.** Discharge curves at different current rates of LFP/Graphite.

Using Figures 16–18, the variation of the specific capacity with the current rate of Li-ion batteries based on LFP/C with the additive of 8% mass of respective activated carbon based on MC (LFP/MC), WH (LFP/WH) and graphite (LFP/graphite) are shown in Table 8. It should be noted that the theoretical specific capacity of LFP is  $170 \text{ mAh} \cdot \text{g}^{-1}$ .

**Table 8.** Variation of the specific capacity with the current rate of Li-ion batteries based on LFP/C with an additive of 8% mass of different activated carbon based on MC (LFP/MC) and WH (LFP/WH). Those of LFP/graphite is also shown.

Sample	Specific Capacity (mAh/g) ( $\pm 2 \text{ mAh/g}$ )			
	Current Rate (C/12)	Current Rate (C/6)	Current Rate (1C)	Current Rate (5C)
LFP/Graphite	167	163	161	120
LFP/MC 1:1	152	148	140	102
LFP/MC 2:1	160	160	157	106
LFP/MC 5:1	149	145	138	100
LFP/WH 1:1	158	155	151	108
LFP/WH 2:1	163	160	157	110
LFP/WH 5:1	153	149	145	106

The results demonstrate, respectively, that activated carbon derived from MC or WH at a KOH/MC 2:1 or KOH/WH 2:1 ratio, exhibits the highest specific capacity and electrical conductivity, surpassing those of the KOH/MC 1:1 and 5:1 or KOH/WH 1:1 and 5:1 samples. This trend is supported by the influence of the KOH activation ratio on the resulting electrochemical and electrical properties of the carbon material.

Among the WH-based cathodes, the LFP/WH 2:1 sample delivers the best specific capacity across multiple current rates. This enhanced performance is attributed to its superior electrical conductivity and well-optimized porous architecture, which jointly facilitates efficient lithium-ion diffusion and improved charge transport kinetics.

These results corroborate the electrical conductivity measurements (Table 5), which had already identified the KOH/WH 2:1 sample as the most effective ratio. Owing to its high electrical conductivity and optimized pore architecture, this material exhibits exceptional electrochemical performance, particularly under high current densities where an increase of efficient ion transport becomes necessary.

#### Cycling Performance of LiFePO<sub>4</sub> (LFP)/C Sample

The electrochemical performance of LFP/C cathodes was assessed through galvanostatic charge/discharge cycling at multiple current rates. The corresponding discharge curves, shown in Figure 19, enable a comparative evaluation of the rate-dependent behavior of each carbon source, highlighting differences in lithium-ion transport efficiency and capacity retention.

LiFePO<sub>4</sub>/C cathodes incorporating activated carbon derived from MC and water WH exhibit a typical decline in specific capacity with increasing current rates of well-documented behavior in lithium-ion battery systems. For MC-based electrodes, this capacity fade becomes more pronounced at elevated rates (1C and 5C), particularly for the LFP/MC 1:1 and LFP/MC 5:1 sample, likely due to kinetic limitations that hinder effective ion and electron transport. In contrast, the LFP/MC 2:1 sample demonstrates superior performance across all tested current rates, benefiting from higher electrical conductivity and improved accessibility to electrochemically active sites.

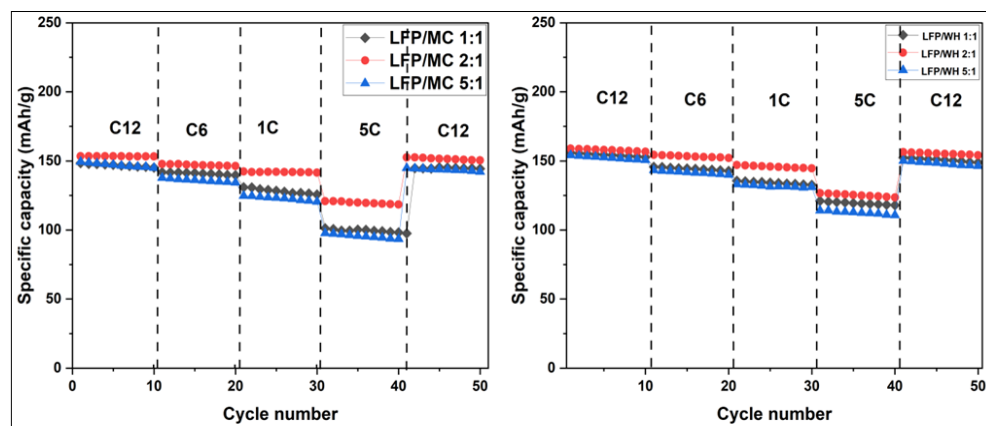


**Figure 19.** Cycling charge/discharge curves at different rates for  $\text{LiFePO}_4/\text{C}$  samples.

A similar trend is observed among WH-based samples, where the LFP/WH 2:1 formulation outperforms both LFP/WH 1:1 and LFP/WH 5:1 counterpart, maintaining higher specific capacities even under high-rate conditions. This enhanced rate capability is attributed to a well-optimized pore structure and elevated conductivity, which together promotes efficient lithium-ion diffusion and facilitates rapid charge transfer processes. This is supported by the results on the study on the interaction of carbon with silicon as anodes for  $\text{LiFePO}_4$  Li-ion battery applications [76]. It was shown that the appropriate design the edge-surface-inter nanocarbon on silicon can be used to form the vertical conductive channels for rapid  $\text{Li}^+$  transport [76].

#### EIS Analysis of $\text{LiFePO}_4/\text{C}$ Cathodes

EIS analysis of  $\text{LiFePO}_4/\text{C}$  (MC, WH) is illustrated in the Nyquist plots (Figures 20 and 21), which represent the relationship between the real ( $Z_{\text{re}}$ ) and imaginary ( $Z_{\text{im}}$ ) components of impedance. These spectra offer valuable insights into the  $R_{\text{ct}}$  and lithium-ion diffusion kinetics. All three spectra corresponding to the LFP/MC and LFP/WH samples exhibit a similar profile: an absent or poorly defined semicircle in the high-frequency region followed by an inclined linear segment at low frequencies (Warburg region), indicative of lithium-ion diffusion within the electrode material, a typical behavior for Li-ion battery systems [77].

Among the MC-based samples, the LFP/MC 2:1 electrode demonstrates the lowest values of both  $R_{\text{e}}$  and  $R_{\text{ct}}$ , suggesting enhanced electronic conductivity and more efficient lithium-ion transport. In contrast, the LFP/MC 5:1 sample exhibits the highest  $R_{\text{ct}}$ , indicating less favorable interfacial kinetics, while the LFP/MC 1:1 electrode displays intermediate behavior. Figure 20 presents the Nyquist plots and the corresponding equivalent circuit models for the LFP/MC cathodes at different KOH/MC mass ratios.

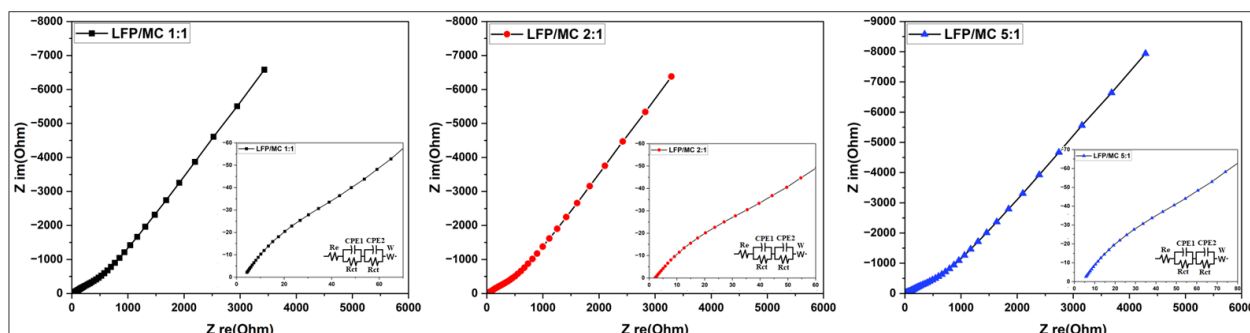


**Figure 20.** Nyquist plot of EIS for  $\text{LiFePO}_4/\text{C}$  (millet cob carbon).

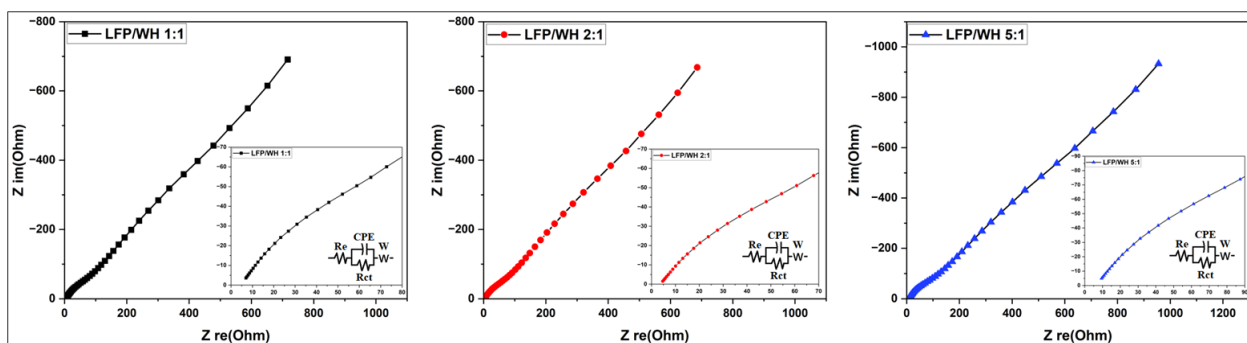


**Figure 21.** Nyquist plot of EIS for LiFePO<sub>4</sub>/C (water hyacinth carbon).

Among the LiFePO<sub>4</sub>/C cathodes (LFP/WH), EIS reveals that the sample prepared with a KOH/WH 2:1 mass ratio exhibits the lowest resistance values. This reflects enhanced electronic conductivity and more efficient lithium-ion transport at the electrode–electrolyte interface. Like the trend observed in MC-derived samples, the LFP/WH 5:1 configuration demonstrates elevated charge transfer resistance, while the LFP/WH 1:1 sample exhibits intermediate electrochemical behavior.

Figure 21 also presents the Nyquist plot for the LFP samples using water hyacinth-derived activated carbon as a support.

The analysis of the influence of KOH/CM mass ratio reveals that a 2:1 ratio offers the optimal balance between electronic conductivity and lithium-ion transport. In contrast, excessive KOH (5:1 ratio) leads to significant degradation of electrochemical performance, likely resulting from structural overactivation and morphological disruption of the carbon framework. Such structural alteration reduces interparticle contact and increases R<sub>ct</sub>. Conversely, a lower ratio (KOH/CM 1:1) promotes excessive microporosity, which impedes charge carrier mobility by restricting ion diffusion during cycling.

Comparative characterization of LFP/C cathodes from LFP/WH and LFP/MC reveals that the WH-based composites exhibit intrinsically lower impedance. This enhancement in electrochemical conductivity may be attributed to differences in the crystalline organization of the carbon matrix. The WH-derived carbon appears to promote more uniform dispersion of LFP particles and facilitate improved electronic percolation pathways.

EIS, analyzed through equivalent circuit fitting, enables extraction of the Warburg coefficient using Equation (3) [77]. This parameter provides quantitative insight into lithium-ion diffusion kinetics. The application of this method highlights the distinct ionic transport behaviors of MC- and WH-based composites, with WH samples exhibiting superior diffusion characteristics. Equation (3) is defined as follows [77]:

$$Z_{re} = R_e + R_{ct} + \sigma_\omega \omega^{-1/2} \quad (3)$$

where: Z<sub>re</sub> is the real impedance, R<sub>e</sub> is the electrolyte resistance, R<sub>ct</sub> is the charge transfer resistance, ω is the angular frequency in the low-frequency range, and σ<sub>ω</sub> represents the slope of Z<sub>re</sub> curve as a function of ω<sup>-1/2</sup>.

To determine the slope of the Z<sub>re</sub> (ω<sup>-1/2</sup>) σ<sub>ω</sub> in Equation (1), we employed a systematic approach by plotting the linear relationship between the real impedance component (Z<sub>re</sub>) and the inverse square root of low-frequency angular frequencies (ω) for the LFP/MC and LFP/WH composites. This linear regression analysis provides a quantitative assessment of the materials' electrochemical behavior, particularly their ionic diffusion dynamics. The resulting fitting lines, displayed in Figure 22, reveal distinct trends for each cathode system, highlighting the superior Warburg-type diffusion characteristics of the WH-derived carbon (LFP/WH) compared to the MC-based counterpart (LFP/MC). Building on the linear

correlations demonstrated in Figure 22, the lithium-ion diffusion coefficients ( $D_{Li}$ ) for the LFP/MC and LFP/WH composites were calculated using Equation (4) given in [78,79]:

$$D_{Li} = 0.5 \left( \frac{R * T}{A * C * \sigma_{\omega} * F^2} \right)^2 \quad (4)$$

where:  $R$  = universal gas constant ( $8.314 \text{ J}\cdot\text{mol}^{-1}\cdot\text{K}^{-1}$ ),  $T$  = absolute temperature (298.5 K),  $A$  = electrode surface area (experimental parameter,  $\text{m}^2$ ),  $C$  is the molar concentration of lithium ions ( $\text{mol}\cdot\text{m}^{-3}$ ),  $F$  = Faraday constant ( $96,500 \text{ C}\cdot\text{mol}^{-1}$ ).

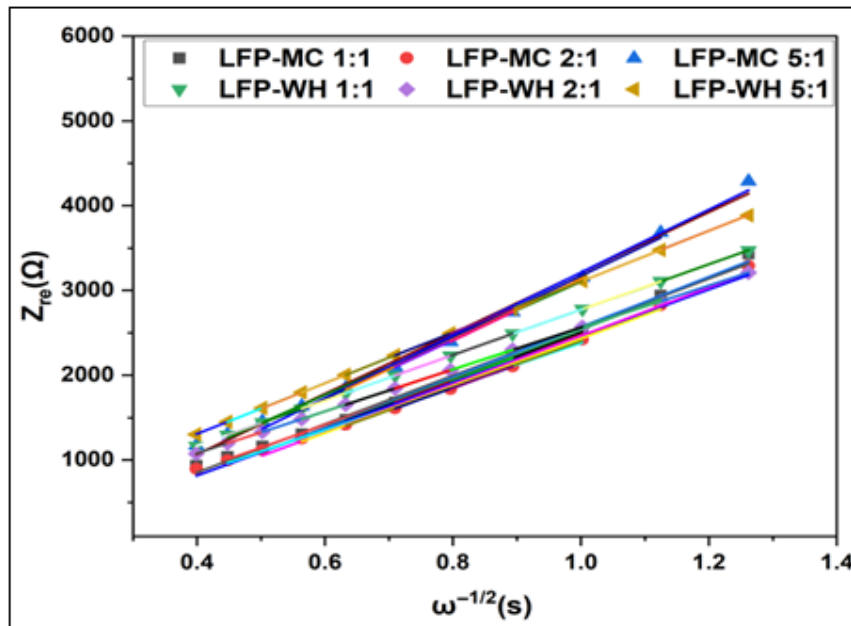


**Figure 22.** Relationship between  $Z_{re}$  and  $\omega^{-1/2}$  at low frequencies of LiFePO<sub>4</sub>/C.

This methodology enables an evaluation of ionic mobility within the cathode materials, directly linking structural properties to electrochemical kinetic performance. The derived  $D_{Li}$  values underscore the superior ion transport efficiency of the WH-based composite, consistent with its enhanced charge transfer dynamics observed in earlier analyses (Figure 22).

The key electrochemical parameters derived from EIS analysis, including  $R_e$ ,  $R_{ct}$ , and  $D_{Li}$ , are shown in Table 9 for the various LFP/MC and LFP/WH cathodes.

**Table 9.** EIS-derived electrochemical parameters for LFP/MC and LFP/WH cathodes.

Samples	$R_e (\Omega) (\pm 0.5)$	$R_{ct} (\Omega) (\pm 0.5)$	$D_{Li} (10^{-13} \text{ cm}^2/\text{s}) (\pm 5\%)$
LFP/MC 1:1	4.4	99.9	1.7
LFP/MC 2:1	2.7	95.9	1.8
LFP/MC 5:1	5.7	124.9	1.0
LFP/WH 1:1	2.7	98.6	1.9
LFP/WH 2:1	2.5	91.1	2.3
LFP/WH 5:1	3.0	110.4	1.5
LFP/graphite	2.3	73.8	3.5

Comparative analysis reveals that the LFP/WH 2:1 composite exhibits the lowest ohmic resistance ( $R_e = 2.49 \Omega$ ) and charge transfer resistance ( $R_{ct} = 91.12 \Omega$ ) among all tested samples. This synergistic improvement corresponds to a notably higher lithium-ion

diffusion coefficient ( $D_{Li} = 2.28 \times 10^{-13} \text{ cm}^2 \cdot \text{s}^{-1}$ ), exceeding values obtained for other configurations. The enhanced ionic transport is attributed to the optimized carbon architecture of the LFP/WH 2:1 electrode, which reduces diffusion path length through a hierarchically porous network, thereby promoting lithium-ion mobility. In contrast, the LFP/MC 5:1 composite, whether derived from millet cob or water hyacinth, exhibits the lowest  $D_{Li}$  values. This limitation is likely due to deficient microporosity and the dominance of poorly connected macropores, which hinder efficient ion percolation. The best values of these respective parameters are obtained with LFP/Graphite.

Graphite, used as a reference material and tested under identical conditions, displays superior electrochemical properties compared to synthesized activated carbon sample.

Figure 23 displays, Nyquist and  $Z_{rc}$  curves of LFP/Graphite. It shows the analysis of the discharge profiles reveals that the LFP/Graphite cathode consistently delivers slightly higher specific capacities across all tested current rates compared to the LFP/WH 2:1 sample. The EIS parameters for this cathode, summarized in Table 9 indicate notably lower values of both  $R_e$  and  $R_{ct}$  relative to the biomass-derived activated carbon electrodes. As a result, the LFP/Graphite cell exhibits the highest  $D_{Li}$ , with the LFP/WH 2:1 sample ranking second. These findings underscore the excellent electrochemical kinetics of graphite while highlighting the promising performance of WH-derived carbon as a viable alternative electrode material.

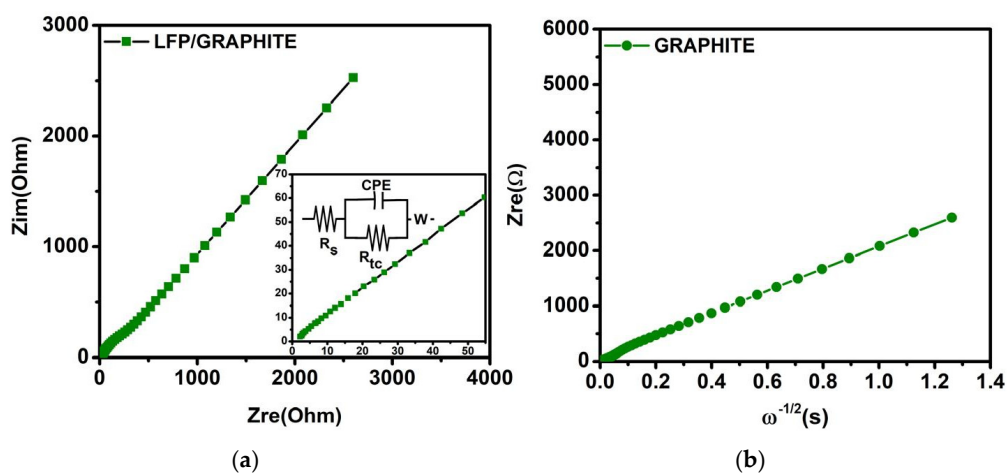


**Figure 23.** Nyquist plot (a),  $Z_{rc}$  ( $\omega^{-1/2}$ ) (b) curves of LFP/Graphite.

### 3.4. Correlation Between the Various Results

Galvanostatic charge/discharge tests demonstrate that, using Lithium anode, the optimum capacities are obtained for the carbons activated at the KOH/CM 2:1, corresponding to the optimum pore structure and pore diameters (Table 6). On the other hand, LiFePO<sub>4</sub> cathodes supported by bio-derived activated carbon achieve specific capacities approaching the theoretical limit of LiFePO<sub>4</sub> (170 mAh·g<sup>-1</sup>), with optimal performance observed in samples activated at a mass ratio KOH/CM 2:1 (Table 8). This ratio offers a favorable balance of pore structure, pore diameter and conductivity, providing pathways for rapid lithium-ion diffusion and efficient electron transport. Notably, carbon derived from WH with its relatively higher crystallinity contributes to superior conductive network formation, enabling enhanced capacity retention across a range of current rates.

Furthermore, Coulombic efficiency stabilizes after the initial cycles (Table 7), indicating successful formation of a stable SEI, which is essential for suppressing parasitic reactions and preserving electrode integrity. In particular, the KOH/WH 2:1 sample display rapid SEI stabilization and sustained high Coulombic efficiency from the second cycle onward, highlighting their potential as effective conductive additives in LiFePO<sub>4</sub>/C sys-

tems. On the other hand, the chemical composition the sample evaluated by EDS (Table 4) and the results on their electrochemical parameters (Tables 6–8, Figures 18 and 23–25) indicate that the best electrochemical performances are obtained with activated biomass containing around 70% of carbon, high content of potassium and high content of silicon. But no evident correlation can be deduced from these results. Further studies are underway to make the possible correlation between the chemical composition and the electrochemical performances.

Cycling stability evaluations of activated KOH/CM carbons reveal excellent capacity retention exceeding 96% of the initial value over multiple cycles (Table 7, Figure 17) for the, KOH/MC or KOH/WH 2:1 sample derived from both MC and WH. These findings underscore the viability of bio-derived activated carbons as cost-effective and environmentally friendly alternatives in lithium-ion battery cathodes. The improved stability is attributed to the synergistic effect of enhanced electrical conductivity and expanded electrochemically accessible surface areas through the crystallinity, pore distribution and size imparted by the biomass carbon.

EIS further supports these observations, indicating relatively low  $R_{ct}$  carbon. Figure 24 presents the correlation between specific capacity and  $R_{ct}$  as a function value for LiFePO<sub>4</sub>/C cathodes incorporating KOH/MC 2:1 and KOH/WH 2:1 activated of the KOH activation ratio.

Among all samples, the KOH/WH 2:1 exhibits the lowest overall resistance, attributed to its well-ordered carbon structure and hierarchical porosity. While a high specific surface area dominated by micropores may limit lithium-ion accessibility, the presence of mesopores is essential for facilitating efficient transport. For example, the KOH/MC 1:1 and KOH/WH 1:1 sample, despite their elevated surface areas, but with small pores sizes, display a higher charge transfer resistance compared to the KOH/CM 2:1 counterpart. These results emphasize the importance of pore size distribution, not just surface area, in determining electrochemical performance. Beyond the optimal KOH/CM 2:1 activation ratio, excessive KOH levels lead to structural degradation manifested as pore over-widening which compromises both capacity and conductivity.

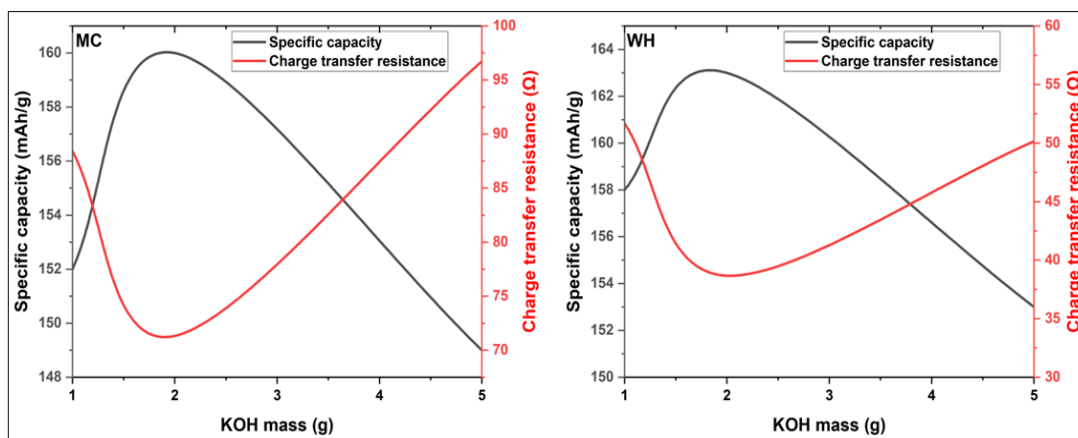


**Figure 24.** Evolution of capacity and charge transfer resistance as a function of KOH Mass.

EIS enabled precise determination of the lithium-ion diffusion coefficients  $D_{Li}$  for LiFePO<sub>4</sub>/C cathodes. Among the samples, the LFP/WH 2:1 composite exhibited the highest diffusion coefficient ( $D_{Li} \approx 2.28 \times 10^{-13} \text{ cm}^2 \cdot \text{s}^{-1}$ ), indicating superior lithium-ion transport kinetics. Interestingly, the KOH/WH 2:1 sample achieved this performance despite having a lower specific surface area than the KOH/WH 1:1 counterpart, emphasizing that  $D_{Li}$  is not solely governed by surface area. Instead, it reflects a confluence of factors, including the electrical conductivity of the carbon matrix, elemental composition affecting charge transfer dynamics, and a well-balanced micro/mesoporous structure that promotes ion mobility.

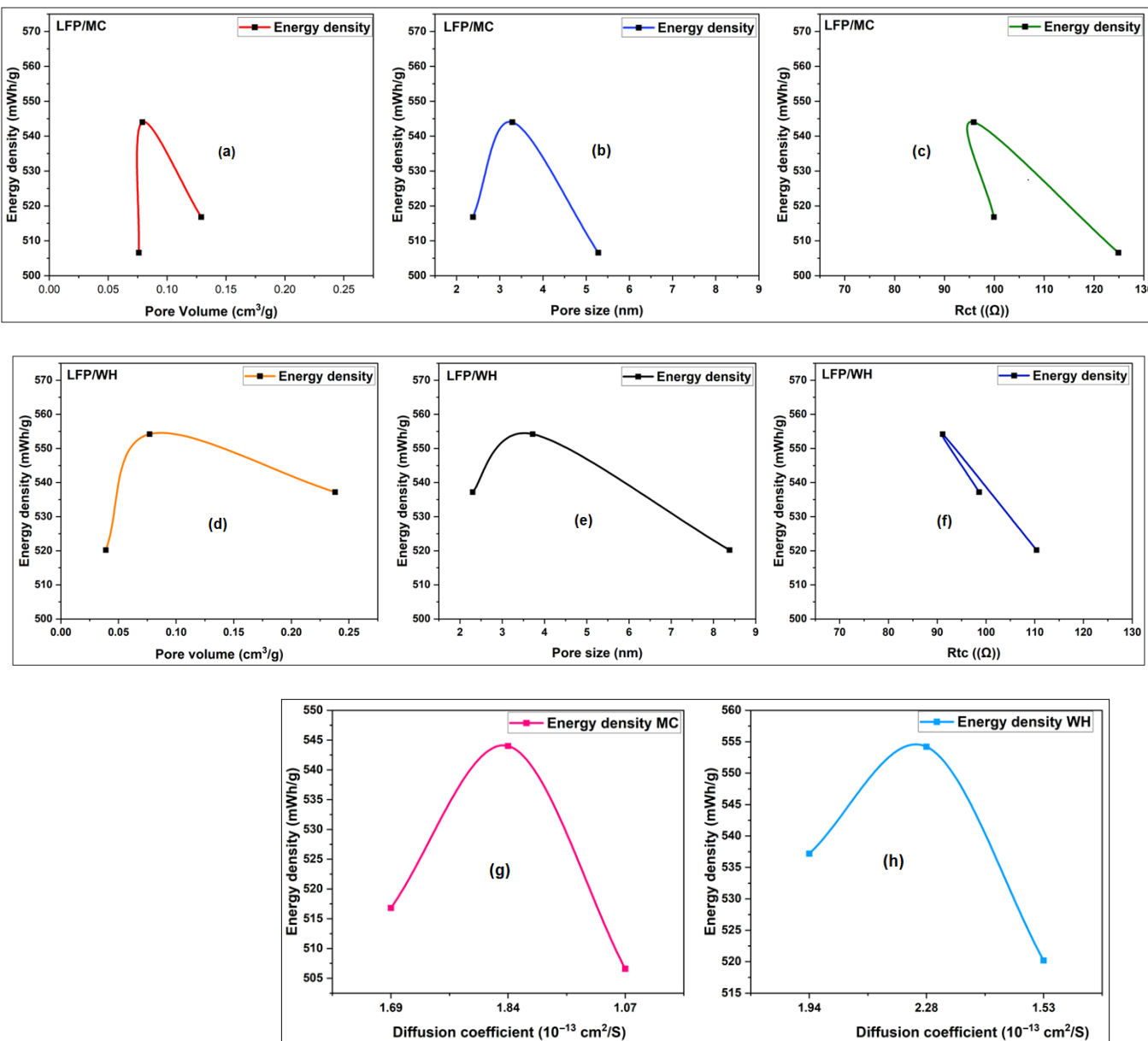


**Figure 25.** Energy density curves as a function: pore volume (a), pore size (b), charge transfer resistance (c) for millet cob, pore volume (d), pore size (e), charge transfer resistance (f) for water hyacinth, diffusion coefficient for millet cob (g) and water hyacinth (h).

In cases where microporosity dominates (>80% of total pore volume), diffusion pathways become constricted, impeding charge carrier mobility and lowering  $D_{\text{Li}}$ . Conversely, a hierarchical pore distribution with an approximately balance micro/mesopore, as observed in the LFP/WH 2:1 electrode, facilitates continuous and accessible ion channels. This structural optimization enhances lithium-ion flux within the composite and reinforces the conclusion that balanced porosity—not maximal surface area—is essential for achieving high-performance lithium-ion battery cathodes.

Furthermore, the energy density curves support and enrich the previous findings. Figure 25 presents, respectively, the energy density curves as a function of pore size, pore volume, charge transfer resistance, and diffusion coefficient for KOH/MC For both studied materials (LFP/MC and LFP/WH), a local maximum in energy density is observed as a function of each of the four key electrochemical parameters: pore size, pore volume, charge transfer resistance ( $R_{\text{ct}}$ ), and diffusion coefficient. These curves highlight the presence of

optimal conditions where the balance between ionic accessibility, active surface area, and charge transport is most favorable. The energy density curves show a maximum energy density relative to the active mass of 544 mWh/g for the LFP/MC 2:1 sample, 554 mWh/g for the LFP/WH 2:1 sample, and 568 mWh/g for the reference LFP/graphite sample. These energy densities were calculated using the capacities obtained from Tables 8 and 9 by the operating potential of 3.4 Volts of Li-ion battery based respectively on KOH/MC, KOH/WH and graphite.

Considering these results, it becomes evident that, to obtain high-performance bio-based activated carbon as a LiFePO<sub>4</sub> cathode additives, several criteria must be met: a high carbon content, both for amorphous or highly crystalline structure. The balanced distribution of micropores and mesopores, and an average pore size greater than 2 nm may lead to good carbon additives for LiFePO<sub>4</sub> cathodes.

#### 4. Conclusions

This study presents a comprehensive evaluation of LiFePO<sub>4</sub> cathodes supported by activated carbon derived from renewable biomass sources, millet cob and water hyacinth. Electrochemical characterizations, including galvanostatic charge/discharge testing, cycling stability assessments, and EIS, collectively revealed outstanding performance, particularly for samples activated at a mass ratio of KOH/carbon 2:1. The LFP/WH 2:1 cathode achieved a specific capacity of 163 mAh·g<sup>-1</sup> at a C/12 rate and retained 110 mAh·g<sup>-1</sup> at 5 C, while the LFP/MC 2:1 sample demonstrated comparable behavior with 160 mAh·g<sup>-1</sup> at C/12 and 106 mAh·g<sup>-1</sup> at 5 C. Across all current densities, these samples exhibited excellent cycling stability, maintaining high capacity retention at elevated rates (1 C and 5 C), further reinforcing their electrochemical robustness.

EIS analysis showed that WH-derived cathodes exhibited lower R<sub>ct</sub> and R<sub>e</sub> compared to MC-based counterparts, confirming the superior electronic conductivity of crystalline carbon obtained from water hyacinth relative to the predominantly amorphous carbon structure in millet cob. This enhanced conductivity, coupled with a more favorable porous architecture, contributes to the superior performance of WH-based cathodes.

Furthermore, activated carbons with moderate specific surface areas and a balance between micropore/mesopore demonstrated optimal performance as conductive support. The presence of interconnected mesopores facilitates efficient lithium-ion diffusion and minimizes charge transport resistance, thereby enhancing overall electrode kinetics. These findings underscore the promise of biomass-derived activated carbon based on millet cob or water hyacinth as sustainable and alternatives to conventional carbon materials, offering a compelling pathway toward high-performance, environmentally friendly lithium-ion batteries.

**Author Contributions:** W.-W.A.Z.: Data curation, all experimental data collections, Writing—original draft. O.S.: Conceptualization, Formal analysis, Supervision, Validation, Writing—review & editing. All authors have read and agreed to the published version of the manuscript.

**Funding:** The research was funded by the National Science and Engineering Research Council of Canada (NSERC) (RGP20002705), UNESCO Chair (FRQ-CUN-338927).

**Data Availability Statement:** Data sets generated during the current study are available from the corresponding author on a reasonable request.

**Acknowledgments:** We thank the National Science and Engineering Research Council of Canada (NSERC) (RGP20002705) for the financial and the Fonds de recherche du Québec, UNESCO Chair (FRQ-CUN-338927).

**Conflicts of Interest:** The authors declare that they have no known competing financial interests or personal relationships that could have appeared to influence the work reported in this paper. The authors declare the following financial interests/personal relationships which may be considered as

potential competing interests: Oumarou Savadogo reports administrative support was provided by Polytechnique Montreal. Oumarou Savadogo reports a relationship with Polytechnique Montreal that includes employment. If there are other authors, they declare that they have no known competing financial interests or personal relationships that could have appeared to influence the work reported in this paper.

## Abbreviations

BET	Brunauer, Emmett, and Teller
BJH	Barrett, Joyner, and Halenda
C	Carbon, Current Rate
CS	Specific Capacitances
D	Diameter
DMAC	Dimethylacetamide
XRD	X-ray Diffraction
EIS	Electrochemical Impedance Spectroscopy
MC	Millet Cob
EDS	Energy Dispersive Spectroscopy
HCl	Hydrogen Chloride
HK	Horváth-Kawazoe
$\text{H}_3\text{PO}_4$	Phosphoric Acid
WH	Water Hyacinth
KOH	Potassium Hydroxide
$\text{LiFePO}_4$ or LFP	Lithium Iron Phosphate
$\text{Li}^+$	Lithium Ion
$\text{LiPF}_6$	Lithium Hexafluorophosphate
CM	Carbonaceous Materials
SEM	Scanning Electron Microscopy
$\text{N}_2$	Nitrogen
NLDFT	Non-Local Density Functional Theory
PVDF	Polyvinylidene Fluoride
$R_{ct}$	Charge Transfer Resistance
$R_e$	Electrolyte Resistance

## References

- Padhi, A.K.; Nanjundaswamy, K.S.; Goodenough, J.B. Phospho-olivines as positive-electrode materials for rechargeable lithium batteries. *J. Electrochem. Soc.* **1997**, *144*, 1188. [[CrossRef](#)]
- Lee, S.; Jang, I.; Lim, H.a.; Aravindan, V.; Kim, H.; Lee, Y. Preparation and electrochemical characterization of  $\text{LiFePO}_4$  nanoparticles with high rate capability by a sol-gel method. *J. Alloys Compd.* **2010**, *491*, 668–672. [[CrossRef](#)]
- Li, Z.; Zhang, D.; Yang, F. Developments of lithium-ion batteries and challenges of  $\text{LiFePO}_4$  as one promising cathode material. *J. Mater. Sci.* **2009**, *44*, 2435–2443. [[CrossRef](#)]
- Balakrishnan, N.T.; Paul, A.; Krishnan, M.; Das, A.; Raphaez, L.R.; Ahn, J.-H.; Jabeen Fatima, M.; Prasanth, R. Lithium Iron Phosphate ( $\text{LiFePO}_4$ ) as High-Performance Cathode Material for Lithium Ion Batteries. In *Metal, Metal-Oxides and Metal Sulfides for Batteries, Fuel Cells, Solar Cells, Photocatalysis and Health Sensors*; Springer: Berlin/Heidelberg, Germany, 2021; pp. 35–73.
- Kim, D.-H.; Kim, J. Synthesis of  $\text{LiFePO}_4$  nanoparticles in polyol medium and their electrochemical properties. *Electrochim. Solid-State Lett.* **2006**, *9*, A439. [[CrossRef](#)]
- Yun, N.J.; Ha, H.-W.; Jeong, K.H.; Park, H.-Y.; Kim, K. Synthesis and electrochemical properties of olivine-type  $\text{LiFePO}_4/\text{C}$  composite cathode material prepared from a poly (vinyl alcohol)-containing precursor. *J. Power Sources* **2006**, *160*, 1361–1368.
- Ritchie, A.; Howard, W. Recent developments and likely advances in lithium-ion batteries. *J. Power Sources* **2006**, *162*, 809–812. [[CrossRef](#)]
- Nakamura, T.; Miwa, Y.; Tabuchi, M.; Yamada, Y. Structural and surface modifications of  $\text{LiFePO}_4$  olivine particles and their electrochemical properties. *J. Electrochem. Soc.* **2006**, *153*, A1108. [[CrossRef](#)]
- Guan, Y.; Shen, J.; Wei, X.; Zhu, Q.; Zheng, X.; Zhou, S.; Xu, B.  $\text{LiFePO}_4$ /activated carbon/graphene composite with capacitive-battery characteristics for superior high-rate lithium-ion storage. *Electrochim. Acta* **2019**, *294*, 148–155. [[CrossRef](#)]

10. Zhang, H.; Liu, D.; Qian, X.; Zhao, C.; Xu, Y. A novel nano structured LiFePO<sub>4</sub>/C composite as cathode for Li-ion batteries. *J. Power Sources* **2014**, *249*, 431–434. [[CrossRef](#)]
11. Wang, H.; Wang, R.; Liu, L.; Jiang, S.; Ni, L.; Bie, X.; Yang, X.; Hu, J.; Wang, Z.; Chen, H. In-situ self-polymerization restriction to form core-shell LiFePO<sub>4</sub>/C nanocomposite with ultrafast rate capability for high-power Li-ion batteries. *Nano Energy* **2017**, *39*, 346–354. [[CrossRef](#)]
12. Tu, J.; Wu, K.; Tang, H.; Zhou, H.; Jiao, S. Mg–Ti co-doping behavior of porous LiFePO<sub>4</sub> microspheres for high-rate lithium-ion batteries. *J. Mater. Chem. A* **2017**, *5*, 17021–17028. [[CrossRef](#)]
13. Talebi-Esfandarani, M. Synthesis, Characterization and Modification of LiFePO<sub>4</sub> by Doping with Platinum and Palladium for Lithium-Ion Batteries. Ph.D. Thesis, École Polytechnique de Montréal, Montreal, QC, Canada, 2013.
14. Wang, B.; Al Abdulla, W.; Wang, D.; Zhao, X. A three-dimensional porous LiFePO<sub>4</sub> cathode material modified with a nitrogen-doped graphene aerogel for high-power lithium ion batteries. *Energy Environ. Sci.* **2015**, *8*, 869–875. [[CrossRef](#)]
15. Jinli, Z.; Jiao, W.; Yuanyuan, L.; Ning, N.; Junjie, G.; Feng, Y.; Wei, L. High-performance lithium iron phosphate with phosphorus-doped carbon layers for lithium ion batteries. *J. Mater. Chem. A* **2015**, *3*, 2043–2049. [[CrossRef](#)]
16. Zhou, Y.; Lu, J.; Deng, C.; Zhu, H.; Chen, G.Z.; Zhang, S.; Tian, X. Nitrogen-doped graphene guided formation of monodisperse microspheres of LiFePO<sub>4</sub> nanoplates as the positive electrode material of lithium-ion batteries. *J. Mater. Chem. A* **2016**, *4*, 12065–12072. [[CrossRef](#)]
17. He, Z.; Zhang, C.; Zhu, Z.; Yu, Y.; Zheng, C.; Wei, F. Advances in carbon nanotubes and carbon coatings as conductive networks in silicon-based anodes. *Adv. Funct. Mater.* **2024**, *34*, 2408285. [[CrossRef](#)]
18. Ali, A.; Cai, R.; Wang, T.; Zhang, C.; Liu, C.; Ma, D.; Hou, H.; Lei, Q.; Xia, Y.; Wang, S. Emerging flexible battery technology: Innovative structural design, material integration and wearable applications and beyond. *Chem. Eng. J.* **2025**, *519*, 165358. [[CrossRef](#)]
19. Wang, Y.; Wang, Y.; Hosono, E.; Wang, K.; Zhou, H. The design of a LiFePO<sub>4</sub>/carbon nanocomposite with a core–shell structure and its synthesis by an in situ polymerization restriction method. *Angew. Chem. Int. Ed.* **2008**, *47*, 7461–7465. [[CrossRef](#)]
20. Huang, H.; Yin, S.-C.; Nazar, L.S. Approaching theoretical capacity of LiFePO<sub>4</sub> at room temperature at high rates. *Electrochim. Solid-State Lett.* **2001**, *4*, A170. [[CrossRef](#)]
21. Shahid, R.; Murugavel, S. Synthesis and characterization of olivine phosphate cathode material with different particle sizes for rechargeable lithium-ion batteries. *Mater. Chem. Phys.* **2013**, *140*, 659–664. [[CrossRef](#)]
22. Chung, S.-Y.; Bloking, J.T.; Chiang, Y.-M. Electronically conductive phospho-olivines as lithium storage electrodes. *Nat. Mater.* **2002**, *1*, 123–128. [[CrossRef](#)]
23. Talebi-Esfandarani, M.; Savadogo, O. Effects of palladium doping on the structure and electrochemical properties of LiFePO<sub>4</sub>/C prepared using the sol-gel method. *J. New Mater. Electrochem. Syst.* **2014**, *17*, 91–97. [[CrossRef](#)]
24. Talebi-Esfandarani, M.; Savadogo, O. Enhancement of electrochemical properties of platinum doped LiFePO<sub>4</sub>/C cathode material synthesized using hydrothermal method. *Solid State Ion.* **2014**, *261*, 81–86. [[CrossRef](#)]
25. Talebi-Esfandarani, M.; Savadogo, O. Synthesis and characterization of Pt-doped LiFePO<sub>4</sub>/C composites using the sol-gel method as the cathode material in lithium-ion batteries. *J. Appl. Electrochem.* **2014**, *44*, 555–562. [[CrossRef](#)]
26. Ravet, N.; Abouimrane, A.; Armand, M. On the electronic conductivity of phospho-olivines as lithium storage electrodes. *Nat. Mater.* **2003**, *2*, 702. [[CrossRef](#)]
27. Shi, M.; Li, R.; Liu, Y. In situ preparation of LiFePO<sub>4</sub>/C with unique copolymer carbon resource for superior performance lithium-ion batteries. *J. Alloys Compd.* **2021**, *854*, 157162. [[CrossRef](#)]
28. Ravet, N.; Besner, S.; Simoneau, M.; Vallée, A.; Armand, M.; Magnan, J.-F. Electrode Materials with High Surface Conductivity. US Patents US6855273B2, 15 February 2005.
29. Chen, Z.; Dahn, J. Reducing carbon in LiFePO<sub>4</sub>/C composite electrodes to maximize specific energy, volumetric energy, and tap density. *J. Electrochem. Soc.* **2002**, *149*, A1184. [[CrossRef](#)]
30. Dominko, R.; Bele, M.; Gaberscek, M.; Remskar, M.; Hanzel, D.; Pejovnik, S.; Jamnik, J. Impact of the carbon coating thickness on the electrochemical performance of LiFePO<sub>4</sub>/C composites. *J. Electrochem. Soc.* **2005**, *152*, A607. [[CrossRef](#)]
31. Doeff, M.M.; Wilcox, J.D.; Kostecki, R.; Lau, G. Optimization of carbon coatings on LiFePO<sub>4</sub>. *J. Power Sources* **2006**, *163*, 180–184. [[CrossRef](#)]
32. Doeff, M.M.; Wilcox, J.D.; Yu, R.; Aumentado, A.; Marcinek, M.; Kostecki, R. Impact of carbon structure and morphology on the electrochemical performance of LiFePO<sub>4</sub>/C composites. *J. Solid State Electrochem.* **2008**, *12*, 995–1001. [[CrossRef](#)]
33. Talebi-Esfandarani, M.; Savadogo, O. Improvement of electrochemical and electrical properties of LiFePO<sub>4</sub> coated with citric acid. *Rare Met.* **2016**, *35*, 303–308. [[CrossRef](#)]
34. Zhi, X.; Liang, G.; Wang, L.; Ou, X.; Gao, L.; Jie, X. Optimization of carbon coatings on LiFePO<sub>4</sub>: Carbonization temperature and carbon content. *J. Alloys Compd.* **2010**, *503*, 370–374. [[CrossRef](#)]

35. Tsuda, T.; Ando, N.; Utaka, T.; Kojima, K.; Nakamura, S.; Hayashi, N.; Soma, N.; Gunji, T.; Tanabe, T.; Ohsaka, T. Improvement of high-rate performance of LiFePO<sub>4</sub> cathode with through-holed LiFePO<sub>4</sub>/Activated carbon hybrid electrode structure fabricated with a pico-second pulsed laser. *Electrochim. Acta* **2019**, *298*, 827–834. [CrossRef]
36. Mwizerwa, J.P.; Liu, C.; Xu, K.; Zhao, N.; Li, Y.; Ndagijimana, P.; Chen, Z.; Shen, J. Activated carbon/reduced graphene oxide wrapped LiFePO<sub>4</sub> cathode for Li-ion batteries with ultrahigh capacities and high specific energy density. *FlatChem* **2022**, *34*, 100393. [CrossRef]
37. Liu, X.; Zhao, R.; Xia, Y.; Li, Q. Improved electrochemical performance of LiFePO<sub>4</sub>/carbon cathode for lithium-ion batteries. *Ionics* **2022**, *28*, 4579–4585. [CrossRef]
38. Han, W.; Zhou, G.; Gao, D.; Zhang, Z.; Wei, Z.; Wang, H.; Yang, H. Experimental analysis of the pore structure and fractal characteristics of different metamorphic coal based on mercury intrusion-nitrogen adsorption porosimetry. *Powder Technol.* **2020**, *362*, 386–398. [CrossRef]
39. Saito, A.; Foley, H. Curvature and parametric sensitivity in models for adsorption in micropores. *AIChE J.* **1991**, *37*, 429–436. [CrossRef]
40. Ravikovich, P.I.; Haller, G.L.; Neimark, A.V. Density functional theory model for calculating pore size distributions: Pore structure of nanoporous catalysts. *Adv. Colloid Interface Sci.* **1998**, *76*, 203–226. [CrossRef]
41. Mikhail, R.S.; Brunauer, S.; Bodor, E. Investigations of a complete pore structure analysis: I. Analysis of micropores. *J. Colloid Interface Sci.* **1968**, *26*, 45–53. [CrossRef]
42. Rouquerol, F.; Rouquerol, J.; Sing, K. Assessment of mesoporosity. In *Adsorption by Powders and Porous Solids*; Academic Press: Oxford, UK, 1999; pp. 191–217.
43. Sohouli, E.; Adib, K.; Maddah, B.; Najafi, M. Manganese dioxide/cobalt tungstate/ nitrogen-doped carbon nano-onions nanocomposite as new supercapacitor electrode. *Ceram. Int.* **2022**, *48*, 295–303. [CrossRef]
44. Sohouli, E.; Adib, K.; Maddah, B.; Najafi, M. Preparation of a supercapacitor electrode based on carbon nano-onions/manganese dioxide/iron oxide nanocomposite. *J. Energy Storage* **2022**, *52*, 104987. [CrossRef]
45. Albo Hay Allah, M.A.; Alshamsi, H.A. Green synthesis of ZnO NPs using Pontederia crassipes leaf extract: Characterization, their adsorption behavior and anti-cancer property. *Biomass Convers. Biorefinery* **2024**, *14*, 10487–10500. [CrossRef]
46. Wilson, G.; Zilinskaite, S.; Unka, S.; Boston, R.; Reeves-McLaren, N. Establishing operando diffraction capability through the study of Li-ion (de) intercalation in LiFePO<sub>4</sub>. *Energy Rep.* **2020**, *6*, 174–179. [CrossRef]
47. Rouquerol, J.; Rouquerol, F.; Llewellyn, P.; Maurin, G.; Sing, K. *Adsorption by Powders and Porous Solids: Principles, Methodology and Applications*; Academic Press: Cambridge, MA, USA, 2013.
48. Barrett, E.P.; Joyner, L.G.; Halenda, P.P. The determination of pore volume and area distributions in porous substances. I. Computations from nitrogen isotherms. *J. Am. Chem. Soc.* **1951**, *73*, 373–380. [CrossRef]
49. Horváth, G.; Kawazoe, K. Method for the calculation of effective pore size distribution in molecular sieve carbon. *J. Chem. Eng. Jpn.* **1983**, *16*, 470–475. [CrossRef]
50. Sing, K.S. Reporting physisorption data for gas/solid systems with special reference to the determination of surface area and porosity (Recommendations 1984). *Pure Appl. Chem.* **1985**, *57*, 603–619. [CrossRef]
51. Yu, S.; Bo, J.; Fengli, L.; Jiegang, L. Structure and fractal characteristic of micro-and meso-pores in low, middle-rank tectonic deformed coals by CO<sub>2</sub> and N<sub>2</sub> adsorption. *Microporous Mesoporous Mater.* **2017**, *253*, 191–202. [CrossRef]
52. Tang, J.; Feng, L.; Li, Y.; Liu, J.; Liu, X. Fractal and pore structure analysis of Shengli lignite during drying process. *Powder Technol.* **2016**, *303*, 251–259. [CrossRef]
53. Rahma, N.A.; Kurniasari, A.; Pambudi, Y.D.S.; Bintang, H.M.; Zulfia, A.; Hudaya, C. Characteristics of Corncob-Originated Activated Carbon Using Two Different Chemical Agent. *IOP Conf. Ser. Mater. Sci. Eng.* **2019**, *622*, 012030. [CrossRef]
54. Wang, S.; Lu, G. A comprehensive study on carbon dioxide reforming of methane over Ni/γ-Al<sub>2</sub>O<sub>3</sub> catalysts. *Ind. Eng. Chem. Res.* **1999**, *38*, 2615–2625. [CrossRef]
55. Kamath, S.R.; Proctor, A. Silica gel from rice hull ash: Preparation and characterization. *Cereal Chem.* **1998**, *75*, 484–487. [CrossRef]
56. Omri, A.; Benzina, M. Characterization of activated carbon prepared from a new raw lignocellulosic material: *Ziziphus spina-christi* seeds. *J. Société Chim. Tunis.* **2012**, *14*, 175–183.
57. Ahmed, S.; Parvaz, M.; Johari, R.; Rafat, M. Studies on activated carbon derived from neem (*Azadirachta indica*) bio-waste, and its application as supercapacitor electrode. *Mater. Res. Express* **2018**, *5*, 045601. [CrossRef]
58. Chen, Y.; Zhu, Y.; Wang, Z.; Li, Y.; Wang, L.; Ding, L.; Gao, X.; Ma, Y.; Guo, Y. Application studies of activated carbon derived from rice husks produced by chemical-thermal process—A review. *Adv. Colloid Interface Sci.* **2011**, *163*, 39–52. [CrossRef] [PubMed]
59. De, B.; Karak, N. A green and facile approach for the synthesis of water soluble fluorescent carbon dots from banana juice. *RSC Adv.* **2013**, *3*, 8286–8290. [CrossRef]
60. Qiu, T.; Yang, J.-G.; Bai, X.-J.; Wang, Y.-L. The preparation of synthetic graphite materials with hierarchical pores from lignite by one-step impregnation and their characterization as dye absorbents. *RSC Adv.* **2019**, *9*, 12737–12746. [CrossRef]
61. Phillips, R.; Jolley, K.; Zhou, Y.; Smith, R. Influence of temperature and point defects on the X-ray diffraction pattern of graphite. *Carbon Trends* **2021**, *5*, 100124. [CrossRef]

62. Barroso-Bogeat, A.; Alexandre-Franco, M.; Fernández-González, C.; Sánchez-González, J.; Gómez-Serrano, V. Electrical conductivity of metal (hydr) oxide–activated carbon composites under compression. A comparison study. *Mater. Chem. Phys.* **2015**, *152*, 113–122. [[CrossRef](#)]
63. Celzard, A.; Marêché, J.; Payot, F.; Furdin, G. Electrical conductivity of carbonaceous powders. *Carbon* **2002**, *40*, 2801–2815. [[CrossRef](#)]
64. Adinaveen, T.; Vijaya, J.J.; Kennedy, L.J. Comparative study of electrical conductivity on activated carbons prepared from various cellulose materials. *Arab. J. Sci. Eng.* **2016**, *41*, 55–65. [[CrossRef](#)]
65. Zhao, H.; Zuo, H.; Wang, J.; Jiao, S. Practical application of graphite in lithium-ion batteries: Modification, composite, and sustainable recycling. *J. Energy Storage* **2024**, *98*, 113125. [[CrossRef](#)]
66. Ryu, S.; Kim, S.; Gallego, N.; Edie, D. Physical properties of silver-containing pitch-based activated carbon fibers. *Carbon* **1999**, *37*, 1619–1625. [[CrossRef](#)]
67. Hashisho, Z.; Rood, M.J.; Barot, S.; Bernhard, J. Role of functional groups on the microwave attenuation and electric resistivity of activated carbon fiber cloth. *Carbon* **2009**, *47*, 1814–1823. [[CrossRef](#)]
68. Huang, Y. Electrical and thermal properties of activated carbon fibers. In *Activated Carbon Fiber and Textiles*; Elsevier: Amsterdam, The Netherlands, 2017; pp. 181–192.
69. Dahn, J.R.; Zheng, T.; Liu, Y.; Xue, J. Mechanisms for lithium insertion in carbonaceous materials. *Science* **1995**, *270*, 590–593. [[CrossRef](#)]
70. Ciosek Höglström, K.; Malmgren, S.; Hahlin, M.; Rensmo, H.; Thébault, F.; Johansson, P.; Edstrom, K. The influence of PMS-additive on the electrode/electrolyte interfaces in LiFePO<sub>4</sub>/graphite Li-ion batteries. *J. Phys. Chem. C* **2013**, *117*, 23476–23486. [[CrossRef](#)]
71. Ekström, H.; Lindbergh, G. A model for predicting capacity fade due to SEI formation in a commercial graphite/LiFePO<sub>4</sub> cell. *J. Electrochem. Soc.* **2015**, *162*, A1003. [[CrossRef](#)]
72. Yang, F.; Song, X.; Dong, G.; Tsui, K.-L. A coulombic efficiency-based model for prognostics and health estimation of lithium-ion batteries. *Energy* **2019**, *171*, 1173–1182. [[CrossRef](#)]
73. Goodenough, J.B.; Park, K.-S. The Li-ion rechargeable battery: A perspective. *J. Am. Chem. Soc.* **2013**, *135*, 1167–1176. [[CrossRef](#)] [[PubMed](#)]
74. Goodenough, J.B.; Kim, Y. Challenges for rechargeable Li batteries. *Chem. Mater.* **2010**, *22*, 587–603. [[CrossRef](#)]
75. Prabaharan, S.S.; Michael, M.S. *Nanotechnology in Advanced Electrochemical Power Sources*; CRC Press: Boca Raton, FL, USA, 2014.
76. Yang, Y.; Wang, J.; Sun, D.; Li, Y.; Xiao, T.; Zhang, C.; Lu, C.; Gao, J.; Xu, C.; Li, Y.; et al. Edge-Surface-Inter Carbon Nanoarchitecture on Silicon. *ACS Nano* **2025**, *19*, 16597–16610. [[CrossRef](#)]
77. Deleebbeck, L.; Veltzé, S. Electrochemical impedance spectroscopy study of commercial Li-ion phosphate batteries: A metrology perspective. *Int. J. Energy Res.* **2020**, *44*, 7158–7182.
78. Cui, Y.; Zhao, X.; Guo, R. Improved electrochemical performance of La<sub>0.7</sub>Sr<sub>0.3</sub>MnO<sub>3</sub> and carbon co-coated LiFePO<sub>4</sub> synthesized by freeze-drying process. *Electrochim. Acta* **2010**, *55*, 922–926. [[CrossRef](#)]
79. Nikgoftar, K.; Madikere Raghunatha Reddy, A.K.; Reddy, M.V.; Zaghib, K. Carbonaceous Materials as Anodes for Lithium-Ion and Sodium-Ion Batteries. *Batteries* **2025**, *11*, 123. [[CrossRef](#)]

**Disclaimer/Publisher’s Note:** The statements, opinions and data contained in all publications are solely those of the individual author(s) and contributor(s) and not of MDPI and/or the editor(s). MDPI and/or the editor(s) disclaim responsibility for any injury to people or property resulting from any ideas, methods, instructions or products referred to in the content.